

Infrared Helium-Hydrogen Line Ratios as a Measure of Stellar Effective Temperature

S.L. Lumsden^{1,3}, P.J. Puxley² and M.G. Hoare¹

¹ Department of Physics and Astronomy, University of Leeds, Leeds LS2 9JT, UK – sll@ast.leeds.ac.uk, mgh@ast.leeds.ac.uk

² Gemini Observatory, 670 N. A'ohoku Place, Hilo, Hawaii 96720, USA – ppuxley@gemini.edu

³ Anglo-Australian Observatory, PO Box 296, Epping, NSW 1710, Australia

23 November 2018

ABSTRACT

We have observed a large sample of compact planetary nebulae in the near-infrared to determine how the $2^1\text{P}-2^1\text{S}$ HeI line at $2.058\mu\text{m}$ varies as a function of stellar effective temperature, T_{eff} . The ratio of this line with HI Br γ at $2.166\mu\text{m}$ has often been used as a measure of the highest T_{eff} present in a stellar cluster, and hence on whether there is a cut-off in the stellar initial mass function at high masses. However, recent photoionisation modelling has revealed that the behaviour of this line is more complex than previously anticipated. Our work shows that in most aspects the photoionisation models are correct. In particular, we confirm the weakening of the $2^1\text{P}-2^1\text{S}$ as T_{eff} increases beyond 40000K. However, in many cases the model underpredicts the observed ratio when we consider the detailed physical conditions in the individual planetary nebulae. Furthermore, there is evidence that there is still significant $2^1\text{P}-2^1\text{S}$ HeI line emission even in the planetary nebulae with very hot ($T_{\text{eff}} > 100000\text{K}$) central stars. It is clear from our work that this ratio cannot be considered as a reliable measure of effective temperature on its own.

Key words: infrared: ISM: lines and bands – ISM: planetary nebulae: general

1 INTRODUCTION

One of the fundamental parameters characterising any stellar population is its mass function, and in particular its *initial* mass function (IMF), defined simply as the number of stars per unit mass that are actually formed in any system. Determining the form of the IMF is vital to our understanding of star formation in our own and other star-forming galaxies, since it allows us to model the chemical and physical evolution of these systems.

Despite ongoing debate (eg. Leitherer 1998) it is not clear whether the IMF varies widely between galaxies or even within different star formation regions of our own galaxy. Since starburst galaxies are generally dusty, IR indicators of the IMF are preferable since they provide considerable improvement in sensitivity since the extinction is lower than in the optical, and perhaps as important, any error in the derived extinction value has a correspondingly smaller effect on any observed line ratio when the lines are close in wavelength. Indeed any method that relies on absolute flux values or widely separated line pairs is likely to lead to significant errors in the derived results when the extinction is large.

There are limited methods for directly measuring the current IMF from stellar features at these wavelengths, so

indirect methods are required. Most work has relied on inferring the nature of the stars present by comparing the ionisation structure of the enveloping nebular gas with the predictions of detailed photoionisation models. There has been extensive use of strong mid and far-IR forbidden line data in modelling HII regions in this fashion. However, such data is difficult to obtain for a large sample of galaxies, the atomic data is typically less certain for forbidden transitions and extinction corrections are complicated by the presence of the silicate absorption feature at $9.7\mu\text{m}$ and our poor understanding of the extinction law at longer wavelengths. Consequently there has not been widespread application of that method.

Given the problems inherent with the longer wavelength forbidden line data, it was natural that attention should turn instead to the near infrared. The brightest lines in general below $2.5\mu\text{m}$ are permitted HI and HeI lines. In principle, the comparison of HeI and HI lines tests the relative volumes occupied by He 0 and He $^+$ relative to H $^+$, and hence places constraints on the form of the emergent UV radiation field shortwards of the HI Lyman limit given the higher ionisation potential of helium. This is certainly true for any lines that arise solely from recombination.

The brightest HeI line longward of $1.1\mu\text{m}$ is the $2.058\mu\text{m}$

HeI 2^1P – 2^1S transition. This has led to considerable attention being given to the use of the ratio of HeI 2^1P – 2^1S with HI Br γ at $2.166\mu\text{m}$ (eg. Doyon, Puxley & Joseph 1992 and references therein). However, the $2.058\mu\text{m}$ HeI 2^1P – 2^1S transition is determined by the population in the 2^1P state. This is largely driven by resonance scattering of the 584\AA HeI 2^1P – 1^1S transition rather than a simple recombination cascade. These resonance photons can be absorbed by dust or hydrogen reducing the population in the 2^1P state. They also depend implicitly on the neutral helium fraction present since they are a resonance from the ground state. In addition, microscopic velocity structure can lead to a sufficient shift in the wavelength emitted so that the photon cannot be reabsorbed by helium at all.

Initially it was thought that these secondary effects were relatively small and easily calculable. However, Shields (1993) showed from a full photoionisation treatment that the strength of the 2^1P – 2^1S line was much more dependent than previously thought on the neutral helium fraction, and indeed predicted that as the stellar effective temperature, T_{eff} , increases much beyond 40000K that this line actually gets weaker as most helium in the HII region is turned into He $^+$. More accurate atomic data and photoionisation models have confirmed this general picture (Ferland 1999). Observational confirmation of this prediction was evident from the extragalactic work of Lumsden, Puxley & Doherty (1994) and Doherty et al. (1995), and the study of planetary nebulae by DePoy & Shields (1994). However, the former papers deal with complex clusters of OB stars for which we have no accurate knowledge of the effective temperature. The latter used slitless spectroscopy of extended planetary nebulae, resulting in very low resolution spectra in which only the brightest lines were visible. Therefore, although we know the trend in the observed data appears to be in accord with the photoionisation models, there have been no attempts to really constrain the model results in any detail.

Crucially, it was still unclear whether or not the HeI 2^1P – 2^1S to HI Br γ ratio can be used as a tracer of the high mass end of the IMF. We therefore decided to carry out observations of objects whose stellar temperature could be defined more accurately than is the case for typical obscured compact HII regions. We observed a sample of 23 planetary nebulae (PN) to derive as full a set as possible of the observable line parameters for both the HeI 2^1P – 2^1S line and HI Br γ . PN are ideal for this test since they are predominantly excited by only a single central star (unlike HII regions), and a sample covering a wider range of effective temperature is much easier to construct.

2 THE PLANETARY NEBULA SAMPLE

Our sample of PN was chosen (i) to be compact on the sky, (ii) to have good quality line measurements in the ESO planetary nebula catalogue (Acker et al. 1992) and (iii) to have a spread in RA to make observation easier. Where possible we chose those objects with predicted Stoy temperatures less than 60000K (Kaler & Jacoby 1991) in preference to hotter objects, but the final sample contains a selection of PN with predicted temperatures well above this value as well. The sample is therefore largely heterogeneous, since our selection criteria do not really distinguish, for exam-

ple, between nearby low temperature and luminosity PN, and more distant high excitation and luminosity PN. In addition, we did not impose any morphological selection on the sample, so there are objects ranging from spherical to bipolar present. For most of our sources there are no published Peimbert types, and even those with published types are often contradictory. It is likely therefore that at least some of our objects are Type I PN, with the consequence that they will probably have enhanced helium abundances (eg Peimbert & Torres-Peimbert 1983). Since we cannot distinguish these PN accurately however, we do not split our sample into Peimbert types. This is not a particular problem for this project however, since all we require is a set of PN with a reasonable spread in effective temperature, which are bright enough that we can derive line ratio measurements easily. We can test for abundance effects by examining the behaviour of the HeI 2^1P – 2^1S line with other helium recombination lines. The only real problem with the inclusion of PN which are not spherical is that the photoionisation modelling reported in Section 5 will not be an ideal match. We do not expect that this will significantly effect the conclusions we reach however.

In addition to our own near infrared spectra we also sought high quality optical data in order to provide more accurate constraints on the photoionisation models. For the most part this comes from a search of the literature, and from the electronic catalogue of Kaler, Shaw & Browning (1997). For some of the PN in our sample we obtained low resolution 4300 – 7400\AA CCD spectra with the red arm of ISIS on the William Herschel Telescope on the night of 30 July 1996 in poor weather. This allowed us to check the reliability of the published data in the literature as well. In particular, we have chosen not to rely on the fluxes from the Acker et al. catalogue in our work beyond the aspect of sample selection wherever possible. The bright lines are often saturated, and the faint HeI lines we require in our analysis are often undetected making the catalogue largely unsuitable if there is an alternative. We also excluded a large amount of the oldest (pre-1980) data since there were clear indications that it disagreed completely with our own CCD data where there were objects in common. Where necessary we placed all data onto a common extinction corrected intensity scale using the extinction law given in Seaton (1979). Since all of the objects (with the exception of CRL 618) have low–moderate optical extinction, we also made the implicit assumption that $A_K = 0$ in our analyses. Since there are no direct means of determining the extinction from the near infrared data alone, we felt this was the safest option. Assuming $A_K = 0$ leads to errors in the observed HeI 2^1P – 2^1S to HI Br γ ratio of $0.1A_K$ or $\sim 0.008A_V$, which are essentially negligible for this sample.

The complete sample is listed in Table 1. We give the optical references we have used there. Also given there are the averaged fluxes of [OIII] 5007\AA , HeI 6678\AA and HeII 4686\AA relative to H β taken from those references. We attribute 10% errors to the relatively weak 6678\AA line, and 5% errors to the others, to account for potential differences in optical and infrared beamsizes when making comparisons of the actual lines. These errors are not included in the analysis of the optical data on its own, since there is no aperture effect to correct for. From these data we have calculated the Stoy temperatures (from the [OIII]/H β ratio and equation

1 of Kaler & Jacoby 1991), electron densities (from the [SII] 6717/6731Å line ratio) and electron temperature (from either the [OIII] 4363/5007Å ratio or the [NII] 5755/6548Å ratio where these exist). These are also given in the Table. Although the density derived from the [SII] doublet is potentially unrepresentative of the density in the He^+ region of the nebula, it is the only indicator that is available for the majority of our sample, and we therefore adopt it throughout.

Unfortunately, as is clear from Table 1, we are lacking in PN with Stoy temperatures between 40000 and 60000K. This was not clear at the time of observation since the predicted values from the ESO Planetary Nebula Catalogue (Acker et al.) did not show this effect. It is only with the adoption of higher quality, and more strictly global, flux values from the literature that it became obvious.

We have included two objects whose identification as PN is uncertain, M 1-78 and CRL 618. The first of these is sometimes listed as a possible HII region, largely on grounds of excitation and extinction. However, there are other confirmed PN with similar characteristics so we have included it in our sample anyway. CRL 618 is more strictly a protoplanetary nebula, since the central source is still obscured, and there is a clear bipolar outflow. Since it will eventually become a PN however, we include it in our sample. It should be noted that the optical data for this object is generally from the bipolar lobes, so may not reflect the actual excitation of the core.

3 OBSERVATIONS

We obtained separate low resolution K band spectra ($R \sim 400$) spanning $\sim 1.9\text{--}2.5\mu\text{m}$, and high resolution echelle spectra around the $2.16\mu\text{m}$ HI $\text{Br}\gamma$ and $2.058\mu\text{m}$ HeI $2^1\text{P}-2^1\text{S}$ lines ($R \sim 20000$) using CGS4, the facility infrared spectrograph on the United Kingdom Infrared Telescope. The data were mainly obtained on the nights of 8 and 9 January 1997, but additional data were also obtained on 15 July 1995, 27 and 28 September 1995, and 4, 5 and 6 July 1997. In all cases we used a two pixel wide slit for the grating spectra, corresponding to 3 arcseconds on the sky. We used a one pixel wide slit for the echelle data to preserve the highest possible velocity resolution. Proper sampling of the spectrum is obtained by stepping the array a fraction of a pixel between ‘sub-exposures’ which are later combined in software to provide the final spectrum. Anamorphic distortion within the spectrograph makes the width of the slit with the echelle grating close to 1 arcsecond.

The separate echelle data of the two lines were obtained primarily for two reasons: first, to derive velocity profiles for the PN to test for the effects of turbulence on the HeI $2^1\text{P}-2^1\text{S}$ to HI $\text{Br}\gamma$ ratio as expected from theory; second, as a means of correcting the low resolution fluxes obtained around $2.058\mu\text{m}$ where there is a sequence of deep narrow atmospheric absorption lines due to CO_2 . However, the echelle data alone cannot be used to derive reliable estimates of the ratio of the HI $\text{Br}\gamma$ and HeI $2^1\text{P}-2^1\text{S}$ lines because we used the narrowest possible slit to maximize the spectral resolution. This means that any small inaccuracy in positioning the telescope can have a significant impact on the derived line ratio given the compact nature of the PN. It is clearly

preferable to derive ratios from lines observed in the same spectrum, so wherever possible we use the low resolution data for this.

The grating spectra were observed in a standard manner, nodding the telescope to keep the source always on the spectrograph slit. The beam separation was between 20 and 30 arcseconds for all data. The data were reduced by dividing by an internal flat field, and coadding all the nod pairs. The data obtained during January 1997 suffered from a problem with the slit mechanism which was tilted markedly relative to the axes of the array. These data were straightened to make the wavelength perpendicular to the columns of the array. The spectra were then extracted, and the negative beam subtracted from the initial positive one. This procedure ensures that residual sky contamination is minimal. The low resolution data were wavelength calibrated in the standard fashion using an argon arc lamp.

Flux calibration of the low resolution data was obtained using observations of a set of A-type stars from the Bright Star Catalogue. We adopted $V - K$ corrections from Johnson (1966) and used the V magnitudes from the Bright Star Catalogue itself. This technique is reliable in providing approximate absolute fluxes (accurate to $\sim 30\%$) and very good ($<< 5\%$) relative fluxes within each spectra which are sufficient for our requirements. The $\text{Br}\gamma$ absorption feature present in the A-type standards was interpolated over using a Lorenzian line profile.

The echelle data were largely obtained in a similar manner, with the exception of the 1997 data. The tilted slit in January 1997 meant that more than one echelle order was present in the final image, so that only the central 20 rows were actually useful for our observations. Therefore we adopted the same strategy as used for mapping extended HII regions described in Lumsden & Hoare (1996), and acquired only one ‘sky’ frame for each set of up to 5 ‘object’ frames. Given the lack of strong sky lines near the emission lines from the PN this procedure provides a reasonable sky subtracted data-set. We used the same technique in July 1997 for simplicity.

For all echelle data there is also a residual distortion in the wavelength calibration due to the fact that the projection of the slit onto the array is actually curved. We used OH night sky lines to ‘straighten’ the spectra for this and the more extreme distortion caused by the tilted slit. We also used the OH lines to provide wavelength calibration for the $\text{Br}\gamma$ data. The HeI data were calibrated using an internal argon arc lamp.

We also acquired spectra of standard stars for the echelle to map the atmospheric absorption features. We used A type standards for the $2.058\mu\text{m}$ data and K type for the $2.166\mu\text{m}$ data, since both are relatively featureless in these wavelength ranges at high resolution. In practice there are only weak atmospheric absorption features around $2.166\mu\text{m}$ so there is little problem with this data. However, around $2.058\mu\text{m}$ the wavelength region is strongly attenuated by a sequence of deep narrow (almost unresolved) atmospheric absorption features due to CO_2 in the upper atmosphere. Although the echelle data can be corrected for this absorption using the standard star observations it reveals a potential problem with the accuracy of the flux calibration in this narrow wavelength range for the low resolution data. The basic argument is simple: given a narrow emission line

as seen in these PN, the actual data as observed through the telescope can range from almost unaffected by the atmospheric absorption to almost completely absorbed. However, the spectra of the standard stars as measured at low resolution average over these absorption features, so that the correction they give to the low resolution data is wrong in most cases.

We used the basic procedures outlined by Doherty et al. (1994) to correct the observed low resolution HeI 2^1P-2^1S fluxes for this atmospheric attenuation. However, rather than using a model of the atmospheric absorption as they did we used the actual observed echelle standard star spectra. First we correct the echelle spectra for changes in the observed radial velocity due to the time of observation. The correction is then derived by smoothing the object and standard echelle spectra to the resolution of the grating data. The smoothed standard star spectrum is used to correct the smoothed PN echelle spectrum, and the flux of the HeI line measured. The original PN echelle spectrum is corrected by the original standard star spectrum as well, and the flux measured of the full resolution data. The ratio of the measured fluxes from the full resolution data with the smoothed data then give the required correction factor. The actual values are given in Table 2. It is worth noting here that no such corrections were applied to the DePoy and Shields (1994) data, potentially leading to errors in their results of up to 30% from this factor alone.

4 THE OBSERVATIONAL DATA

4.1 The Spectra

The spectra acquired with the echelle grating are shown in Figures 1 and 2. The full set of low resolution spectra will be published separately in a paper that discusses the other spectral features present. However, a representative sample showing the trend with effective temperature are shown in Figure 3. In all cases we have summed up the data over the whole object in forming these spectra.

The observed HI Br γ fluxes are listed in Table 2, along with the ratios of the strongest helium lines with Br γ . The tabulated values of HeI 2^1P-2^1S against HI Br γ are all corrected for atmospheric absorption using the method given in Section 3. All ratios are taken from the low resolution data with the exception of the HeI $7^{1,3}G-4^{1,3}F$ transition at $2.16475\mu m$, which was measured from the echelle spectra. This is the strongest of the HeI satellite lines to Br γ , and is visible in most of our echelle spectra. The ratio given for that line is against the observed Br γ flux from our echelle spectra. This line can also be compared with the other HeI lines, since they would all arise from the same region of the PN. It should not however be compared with the HeII line strengths, since they will come from a different region in the PN, and the possible differences in slit position and size again may come into play. Also visible in some of the Br γ echelle spectra are the other HeI transitions of 7^1F-4^1D at $2.16229\mu m$ and 7^3F-4^3D at $2.16137\mu m$, and the HeII 14–8 transition at $2.1653\mu m$. It should be noted that the low resolution Br γ data have not been corrected for any underlying HeII emission (the bright satellite HeI lines are sufficiently well resolved not to contribute to the measured fluxes). Examination of the echelle spectra shows that these lines are

insignificant for most of the sample, and even for the higher excitation PN contribute at most 5% of the flux. The one exception is Hu 1-2, which shows evidence for a bipolar flow and enhanced helium abundance indicating it may be a Type I PN. For this case, the HeII lines may contribute up to 10% of the observed low resolution Br γ flux.

We also used the echelle data to derive line widths for the HI Br γ and HeI 2^1P-2^1S lines. We used Gaussian fits in all cases. The results are given in Table 3. Where the fit deviated noticeably from a single Gaussian, we note this below in Section 4.3, and in the Table by including the separate Gaussian components required to achieve a good overall fit. We also measured the widths of isolated OH night sky lines to determine the instrumental resolution, since these lines are significantly narrower than this. The instrumental widths changed by no more than 10% between the different observing sessions (the worst data being that obtained in January 1997 due to the problems with the slit mechanism). In all cases, the HeI data is higher resolution than the equivalent Br γ data. The intrinsic linewidth for each observation was derived assuming the intrinsic and instrumental widths added in quadrature. The values give in Table 3 have been corrected for the instrumental resolution.

4.2 Optical and Infrared Line Ratios

The observed linear correlation between the [OIII] $5007\text{\AA}/H\beta$ line ratio and the Stoy temperature found by Kaler & Jacoby (1991) implies that we can look for trends in our data in an entirely model independent fashion by examining the correlation between infrared line ratios and the [OIII]/H β ratio. The basic results of our survey then are shown in Figure 4. Figure 4(a) shows the ratio of the HeI $7^{1,3}G-4^{1,3}F$ and Br γ against the [OIII] $5007\text{\AA}/H\beta$ line ratio. The result is the expected one in the sense that the volume of the He $^+$ region rises rapidly with effective temperature ([OIII] line strength) until it fills the entire PN. In Figure 4(b) we show the ratio of HeI 2^1P-2^1S and Br γ against the [OIII] $5007\text{\AA}/H\beta$ line ratio. Here there is a much less well defined trend with increasing [OIII]/H β ratio, as expected if the results from previous photoionisation models are correct. In particular we note two key points: this ratio peaks at lower effective temperature than the HeI $7^{1,3}G-4^{1,3}F$ to Br γ ratio and it decreases with increasing [OIII]/H β ratio beyond this peak, both of which are in accord with the models presented by Ferland (1999).

We can test whether we have introduced any bias in these results from combining the optical data from the literature with our observed infrared data by further examining the behaviour of helium-to-hydrogen line ratios in the optical and infrared separately. In Figure 5(a) we plot the ratio of 6678\AA HeI 3^1D-2^1P transition with H β against HeI $7^{1,3}G-4^{1,3}F$ with Br γ . Smits (1996) determined values of expected line emissivities for high- n states such as the HeI $7^{1,3}G-4^{1,3}F$ lines, as well as the more common optical lines in the general recombination case, including collisional effects amongst the lowest levels. Benjamin, Skillman & Smits (1999) expanded this treatment of the collisional effects to higher levels, and detail the resultant emissivities of the better known lines, but otherwise recover the same data for the pure recombination case. The two solid lines in Figure 5(a) show the full range of possible theoretical values

for $n_e = 10^2 - 10^6 \text{ cm}^{-3}$ and $T_e = 10000 - 20000 \text{ K}$ from the Smits (1996) data. All of the $3^1\text{D}-2^1\text{P}$ and $7^{1,3}\text{G}-4^{1,3}\text{F}$ lines should be dominated by recombination processes. Line opacity and collisional excitation, which can affect the lower lying triplet states significantly, should be relatively unimportant here. Figure 5(a) clearly indicates that this is the case, since there is a well defined linear relation between the two ratios which is in reasonable agreement with the predicted theoretical values.

It is interesting to compare this with Figure 5(b), in which we plot the same optical ratio against the ratio of $\text{HeI } 4^{1,3}\text{S}-3^{1,3}\text{P}$ with $\text{Br}\gamma$. Again the straight lines show the expected theoretical values for the range $n_e = 10^2 - 10^6 \text{ cm}^{-3}$ and $T_e = 10000 - 20000 \text{ K}$ (assuming no collisional excitation). There is a larger theoretical dispersion in this instance, largely due to a stronger dependence of the $\text{HeI } 4^{1,3}\text{S}-3^{1,3}\text{P}$ line fluxes on electron temperature. Despite this, there is a clear trend for some points to lie well away from the theoretical values, in the sense that the $4^{1,3}\text{S}-3^{1,3}\text{P}$ blend is brighter than expected from recombination alone. These are clearly objects in which the population of the 4^3S level of HeI is enhanced. This can be due to either collisional excitation (largely from $2^3\text{S}-4^3\text{S}$) or opacity in the $2^3\text{S}-n^3\text{P}$ series (leading to corresponding enhancements in the S-P series). The relative contribution of the two can be estimated from the atomic data (eg Lumsden & Puxley 1996) and for the typical conditions of the PN in this survey they contribute almost equally since it is primarily density that drives both effects. The role of collisions have also been calculated more exactly for HeI emission in general by Benjamin, Skillman & Smits (1999) as noted above. They find enhancement of order 50% in the $4^3\text{S}-3^3\text{P}$ line is possible for the physical conditions being considered, in accord with our data. The PN that lie away from the linear trend are obvious from Table 2 from a comparison of the $\text{HeI } 4^{1,3}\text{S}-3^{1,3}\text{P}$ and $\text{HeI } 7^{1,3}\text{G}-4^{1,3}\text{F}$ fluxes, since these should be similar in the presence of recombination alone. However, there does not appear to be a clear correlation between these objects and their electron density as would be expected. This suggests that the estimated densities from the [SII] doublet are not entirely reliable. In particular, all of the PN showing HeII emission appear to show this effect. In such objects of course the S^+ zone will lie at the edge of the nebula, which may not be representative of the nebula as a whole. In many cases there is evidence for higher densities in the literature, as estimated from [OII] lines. This is consistent with the simple model in which the [SII] emission arises at the edge of the nebula since O^+ has a higher ionisation potential than S^+ .

4.3 Velocity Structure

As noted in the introduction purely local velocity broadening of the $584\text{\AA} 2^1\text{S}-1^1\text{S}$ HeI resonance line can reduce the likelihood of absorption by neutral helium (cf Ferland 1999), and hence reduce the ratio of the $\text{HeI } 2^1\text{P}-2^1\text{S}$ and $\text{HI } \text{B}\gamma$ lines. In the on-the-spot approximation for emission and absorption of this resonance line, only local broadening processes count, since no 584\AA photon will travel a sufficient distance for a global velocity field to be an important factor. We therefore need a measure of the local broadening if we are to compare our data with the correct photoionisation model.

Therefore we have assumed a simple model to decompose the observed line width into local and global velocity broadening with the PN. We assume that the intrinsic line width is determined by three possible factors: the expansion velocity of the nebula, the thermal line width, and turbulence, the first of these being the only purely global broadening mechanism. We also assume that the expansion velocity has a particularly simple form, namely a constant value everywhere in the nebula. Although unrealistic in practice, the variation in expansion velocity is generally sufficiently small that we can ignore it here. The profile locally will appear Gaussian, with the broadening as given by equation 2 below. Along a line of sight directly through the centre of the shell we would then see the classic split line profile composed of two Gaussians offset from each other by twice the expansion velocity.

However since the the objects are compact (mostly unresolved) on the sky we see total velocity field in the beam. The velocity profile is ‘infilled’ from those regions of the nebula where the velocity field is more perpendicular to the line of sight than tangential, so that the double profile will not be evident in the actual observed data. If we integrate this velocity profile over the whole extent of the PN, then we can derive the observed profile, which is given by (for an unresolved source)

$$I(v) \propto \int_V j(\mathbf{r}) \exp(-((\mathbf{v} - \mathbf{v}_{exp}) \cdot \mathbf{n})^2 / 2\sigma_v^2) dV \\ \propto \text{erf} \left(\frac{v + v_{exp}}{\sqrt{2}\sigma_v} \right) - \text{erf} \left(\frac{v - v_{exp}}{\sqrt{2}\sigma_v} \right) \quad (1)$$

where j is the emissivity as a function of position in the nebula (which we assume here is constant), \mathbf{v}_{exp} is the expansion velocity so that $\mathbf{v}_{exp} \cdot \mathbf{n} = v_{exp} \cos \theta$ if \mathbf{n} is the vector defining our line-of-sight, and

$$\sigma_v^2 = \frac{1}{2} \left(\frac{2kT}{m_{ion}} + v_{turb}^2 \right). \quad (2)$$

For a nominal $T_e = 10000 \text{ K}$, and no turbulence, $\sigma_v \simeq 9.1 \text{ km s}^{-1}$ for HI and $\simeq 4.6 \text{ km s}^{-1}$ for HeI . In the absence of expansion, the line profile will be Gaussian, and the broadening is given solely by equation 2.

For most of the objects considered here, the actual derived profile is sufficiently similar to a Gaussian that we cannot uniquely determine the split between turbulence and global expansion. We can estimate the thermal line width directly from the derived electron temperature in each region to remove that uncertainty. In practice therefore the best discrimination comes from a comparison of the differences in the observed widths for the HI and HeI lines. We calculated the widths of the lines for varying values of v_{exp} and v_{turb} and sought the ‘best’ match from this grid of data. An example for $T_e = 10000 \text{ K}$ is shown in Figure 6. For the HI and HeI separately we find the set of curves that match the observed data. These then give the derived v_{turb} and v_{exp} values shown in Table 4. Since a family of curves is possible in almost all cases only upper limits to v_{turb} and v_{exp} can be derived. Clearly, however, these are not joint limits, since when v_{turb} is large v_{exp} must be small and vice-versa. For some of the objects there is a discrepancy between the values derived from the HI and HeI lines. In some cases this is due to the fact that the He^+ and H^+ zones do not over-

lap because the effective temperature of the exciting star is too low. For these objects we use the limits on the HeI line alone. For a small sample of objects there are no reliable solutions within the context of our simple model. Comments on these objects are given below, together with other notes on individual PN.

BD+30°3639: there is considerable structure in BD+30°3639 (cf Sahai & Trauger 1998). The split in the two components seen in the HeI line give $v_{exp} \sim 30 \text{ km s}^{-1}$ in terms of our simple model, so no turbulent broadening is required. This expansion velocity is not however compatible with the HI line data. It seems likely that our simple model is not a good approximation for this source. However, even given this, there appears little need to invoke a large turbulent velocity component.

CRL 618: The spectra acquired for this paper were centred on the brighter of the two outflow lobes visible in the optical. The actual HII region is in fact completely obscured at optical wavelengths. Our data agree with previous published near infrared data (Hora, Latter & Deutsch 1999), which also seems to have been centred on the visible lobe rather than the actual core. We have further low resolution data that will be published separately of the core showing strong HI emission, and stronger HeI emission than present in the lobes. However, since we have only obtained echelle spectra of the lobe position we only quote the result for the HI and HeI line strengths there. It is possible that most of the emission we detect in the lobes is actually scattered light from the obscured central regions, since CRL 618 is known to have significant polarisation. Trammell, Dinerstein & Goodrich (1993) show that, in the optical, all the recombination lines and high excitation forbidden lines are scattered into our line of sight. We therefore do not attempt to determine turbulent or expansion components to the velocity from the observed data (which would imply very large velocities), and for sake of the photoionisation model simply assume $v_{turb} \sim 10 \text{ km s}^{-1}$.

Hu 1-2: this object shows clear signs of a bipolar outflow in the echelle spectra, rather than straightforward expansion, since the velocity field flips from red to blue shifted moving south across the position of the central star. The double peaked line profile that results is clearly visible in both echelle spectra. The difference in line width probably reflects a differing acceleration in the He⁺⁺ and He⁺ zones in the outflow. The observed widths limit $v_{turb} \leq 10 \text{ km s}^{-1}$.

M 1-1: Only a two component Gaussian fit gave a good match to the data. The velocity separation of the two peaks is $\sim 58 \text{ km s}^{-1}$, indicating an expansion velocity of $\sim 30 \text{ km s}^{-1}$. The predicted turbulent velocity component is then small, since most of the remaining line broadening must be thermal. Because of the weakness of the HeI 2¹P–2¹S line in the low resolution data we did not observe this object with the echelle at 2.058 μm . There are no satellite HeI lines visible in the Br γ data either.

NGC 7027: this is the only one of our sample to show spatially resolvable velocity structure. The structure most closely resembles an expanding shell in agreement with the radio data of Roelfsema et al. (1991). Given this we can further limit the velocity components so that $v_{exp} \sim 20 \text{ km s}^{-1}$ and $v_{turb} \leq 10 \text{ km s}^{-1}$.

5 PHOTOIONISATION MODELS

5.1 Basic Parameters

We used Cloudy version 90.05 (Ferland 1996) to model the emission line spectra for a grid of PN with differing physical parameters. The main parameters we considered were effective temperature, central star luminosity, electron density and the velocity structure. All models used the standard Cloudy planetary nebula abundances with their corresponding dust grain abundance.

We considered effective temperatures in the range 25000–150000K. We used two sets of model atmospheres. First, to ensure that we have the same model for all temperatures, we used a simple blackbody approximation. Then, to test whether a different model might affect the results, we used the standard Kurucz (1992) models with $\log g = 5$ for the more restrictive temperature range of 25000–50000K. The only alternative models of stellar atmospheres potentially applicable to low effective temperature PN in the version of Cloudy used are due to Mihalas (1972). We did not consider these however when it became clear that the blackbody models were a sufficiently good match to our data (see Section 5.2).

There is observational and theoretical evidence that PN central stars with low effective temperatures all have approximately the same bolometric luminosity. Observational evidence comes from studies of PN in the Magellanic Clouds (cf Figure 11 in Dopita et al. 1996). The theoretical model tracks of Vassiliadis & Wood (1993) also show that below 50000K there is little dispersion in the luminosity-effective temperature domain. From Vassiliadis & Wood (1993) we adopt a value of $5000 L_\odot$ as a mean bolometric luminosity, but consider 3000 and $7000 L_\odot$ as well, since these match the spread in the range of observed and theoretical values for PN central stars below about 100000K. The range of electron density and turbulent/expansion velocity considered are taken directly from the observed data. We computed models with $n_e = 3000, 6000, 12000, 24000$ and 48000 cm^{-3} , and $v_{turb} = 0, 5, 10$ and 15 km s^{-1} .

Lesser effects that need to be considered are due to metallicity/abundance and the final radius chosen. This latter parameter is really only important for the PN with hot central stars, since, for small outer radii, the nebula can be density rather than ionisation bounded, resulting in reduced He⁺ zones. This is apparent in some of the observed data for those PN with hot central stars. Since it only affects the high temperature end of the models, we adopt $r_{out} = 0.1 \text{ pc}$ as an appropriate value for our sample (cf the values in Cahn, Kaler & Stanghellini 1992), and accept that this may mean that we overestimate the model HeI line strength at high effective temperature. The inner radius has little effect on the strengths of the lines we are interested in, and we adopt $r_{in} = 0.01 \text{ pc}$. We do not consider metallicity effects further here, since there is no direct evidence from the observational data that it is a significant effect. For example, DdDm 1 is a known halo PN, which has lower metallicity than the other PN in the sample, but whose helium-to-hydrogen line ratios show little deviance from the rest of the sample.

5.2 Model Results

Our selection used the relation between the [OIII] 5007Å to H β ratio and Stoy temperatures for the PN central stars as derived by Kaler and Jacoby (1991) to determine approximate stellar effective temperatures for our sample. However, these temperatures are not completely reliable measures of the actual underlying T_{eff} , since the method is only sensitive to effective temperatures below 60000K. This can be seen clearly in Figure 7, where we show the original data used by Kaler & Jacoby, together with their fit to the same data, and the results from our photoionisation modelling. It is encouraging that the blackbody stellar models reproduce the spread in the observed data reasonably well. In this case it appears that the identification of the underlying effective temperature with the Stoy temperature is sound up to 60000K. This is in spite of the fact that a black body is not a good match to the actual spectrum of a PN central star. However, previous workers have also found that their use gives a good match between model and observation (cf. the discussion in Dopita & Meatheringham 1991). By comparison, the Kurucz model atmospheres which are shown as the dashed line in Figure 7 do not reproduce the observed relation at all, particularly at the lower end of our effective temperature range (note also that the Kurucz models only exist for $T_{eff} < 50000$ K). We therefore did not consider the further use of these models. The primary mechanism giving rise to the spread in [OIII] 5007Å to H β ratio at a fixed temperature is the electron density. Collisional enhancement at a fixed temperature can change the ratio by 30% over the range of densities considered (the largest value of the ratio occurring at $n_e = 20000\text{cm}^{-3}$; at higher values the ratio declines again), whereas the central star luminosity contributes at most a 15% change, and the velocity structure is essentially irrelevant.

As can be seen, the [OIII]/H β ratio rises almost linearly with temperature, as the O $^{2+}$ region in the nebula increases in size, until about $T_{eff} = 60000$ K. However, beyond this temperature, the O $^{2+}$ region saturates, and eventually decreases with increasing T_{eff} as O $^{3+}$ becomes dominant. In addition, for our sample of compact PN, it is possible that the nebula is density rather than ionisation bounded. This effect tends to become significant for temperatures above that at which the He $^{++}$ region first appears (~ 50000 K). For a compact nebula, the available gas reservoir at this point may be less than that required to absorb all the emitted radiation below 912Å. In this case, the flux from the lower ionisation species near the edge of the nebula will clearly drop first. The effect is the same as that which leads to the well known difference between hydrogen and helium Zanstra temperatures in PN at high temperature (cf Kaler & Jacoby 1991 and references therein). Therefore for those PN showing evidence of HeII emission we deduced a calibration between the 4686Å HeII line strength and T_{eff} from the models. First, we extended the effective temperature range by calculating a small set of models spanning the range 150000–400000K, with $L_* = 5000\text{L}_\odot$, $n_e = 12000\text{cm}^{-3}$ and $v_{turb} = 5\text{km s}^{-1}$. Variations in the luminosity and density lead to changes of less than 25% in the 4686Å HeII to H β ratio. We interpolated these data to find effective temperatures for the real PN. There was one problem with this approach, since the model HeII 4686Å to H β ratio never increased beyond 0.55

(near 30000K: again this is a reflection of the fact that the He $^{++}$ zone is now becoming density bounded). Three of our PN show values larger than this however. This may be a reflection of either a density bounded nebula or non spherical geometry. For the sake of this paper we simply ascribe to these PN a lower limit on the effective temperature of 25000K.

In Figure 8 we show how the HeI 2¹P–2¹S to HI Br γ ratio varies as a function of effective temperature. We have explicitly split the dependence on (a) density, (b) turbulent velocity and (c) stellar luminosity to show how the ratio is affected by each. The results are as expected. The ratio increases with increasing density because of collisions from the metastable 2¹S state enhancing the population of the 2¹P state. As the microscopic velocity width increases, the 584Å 2¹P–2¹S resonance line weakens, leading to a decrease in the population of the 2¹P state. As the stellar luminosity increases the ionisation parameter at the inner edge of the cloud also increases, leading to a marginal increase in the He $^{++}$ region compared to a lower luminosity star, once that star is hot enough to actually excite this state, and a decline in the fraction of He 0 and He $^+$. Since He 0 is required to scatter the 584Å photons, the direct consequence is a reduction in the ratio for effective temperatures beyond about 40000K. From Figure 8 it is also clear that the models with the ‘extreme’ high and low ratios are those with high density, and low turbulent velocity and central star luminosity and low density, and high turbulent velocity and central star luminosity respectively. Since the luminosity dependence is only weak however, we will ignore it in the following, and consider only our mean central star luminosity of $L_* = 5000\text{L}_\odot$.

5.3 Comparison with Observations

All of the strong HI and HeI lines are calculated directly by Cloudy, but the two weaker K band HeI lines are not. Since the 2.16475μm 7^{1,3}G–4^{1,3}F line must be dominated by recombination processes, and the 6678Å 3¹D–2¹P is known to be (eg Benjamin et al. 1999), the ratio of these two lines must in theory be roughly constant. Figure 5(a) shows that this is true observationally. We can therefore use the data from Smits (1996) to correct the model 6678Å flux into a model 2.16475μm flux. The actual correction for $T_e = 10000$ K and $n_e = 10000\text{cm}^{-3}$ is that the model HeI 7^{1,3}G–4^{1,3}F to HI Br γ ratio is 1.23 times the model HeI 3¹D–2¹P to H β ratio (where we have also used the data on HI from Storey & Hummer 1995). This values rises to 1.31 for $T_e = 20000$ K and $n_e = 10000\text{cm}^{-3}$. The value depends only slightly on electron density but much more strongly on electron temperature.

Unfortunately, the behaviour of the 2.113μm 4^{1,3}S–3^{1,3}P line is not as simple to translate from the Cloudy results, given the comments in section 4.2. We therefore chose not to compare it to the model, but rather to use its ratio with the 7^{1,3}G–4^{1,3}F line as an indicator of collisional or line opacity effects, and hence of high electron density ($> 10^4\text{cm}^{-3}$). As noted in Section 4.2, these objects can be found in Table 2 by a comparison of the HeI 4^{1,3}S–3^{1,3}P and 7^{1,3}G–4^{1,3}F fluxes. Objects with significantly larger 4^{1,3}S–3^{1,3}P fluxes than 7^{1,3}G–4^{1,3}F fluxes must have enhanced 4³S populations, and hence high electron density.

In Figure 9(a) we plot the observed HeI 7^{1,3}G–4^{1,3}F to

HI Br γ ratio and in Figure 9(b) the observed HeI 6678Å 3¹D–2¹P to H β ratio as taken from the literature. We also plot a typical result from our photoionisation models (the actual results change by less than 5% as a function of density, luminosity or velocity, and 10% as a function of electron temperature). We have not labelled the individual PN here since clearly both sets of data are in good agreement with the models. Therefore we can be confident that the ratio of a pure recombination HeI and HI line does behave in the fashion expected, and that such a ratio could be used as a measure of effective temperature in the 30–40000K range.

In Figure 10 we plot the observed HeI 2¹P–2¹S to HI Br γ ratio against effective temperature (taken to be the greater of T(Stoy) or T(HeII) from Table 1). The solid lines are the model results for the ‘extreme’ models for a central star with a luminosity of 5000 L $_{\odot}$ as discussed in the previous section. The lower curve is a model with $n_e = 3000\text{cm}^{-3}$ and $v_{turb} = 15\text{km s}^{-1}$ and the upper curve is a model with $n_e = 48000\text{cm}^{-3}$ and $v_{turb} = 0\text{km s}^{-1}$. We have labelled the individual PN to make identification easy. We have compressed the temperature scale to show the detail at $T_{eff} < 50000\text{K}$, but note that the high excitation PN that are not plotted all lie above the predicted model curve. Finally in Figure 11 we plot the observed HeI 2¹P–2¹S to HeI 7^{1,3}G–4^{1,3}F ratio, since this removes any metallicity dependence. We have plotted the same models as in Figure 10.

From Figure 10, it is clear that the models systematically underpredict most of the high effective temperature PN. These objects do show evidence for high density (either from their [SII] ratios, or from the strength of the HeI 4^{1,3}S–3^{1,3}P line). Some must have low turbulent velocities (M 1-20 for example), but there does not appear to be a clear trend of the ratio with this parameter (remembering from Figure 8 that even turbulent velocities at the 10km s $^{-1}$ level will suppress the HeI 2¹P–2¹S line by 25% at high T_{eff}). Indeed 3 of the sources shown in Figure 10 and 11 (M 1-20, K 3-62 and M 1-4) lie above the maximum predicted theoretical values for the ratios shown, and the same trends also carry through to the higher effective temperature PN not plotted in Figures 10 and 11. From Figure 11 it is also clear that enhanced helium abundance cannot explain the observed data for these objects, since they also tend to lie above the model predictions there. For effective temperatures near and above 60000K it is also clear from Figure 8 that density has only a small role in determining the HeI 2¹P–2¹S line strength. Therefore higher density than that used in our modelling is also unlikely to account for these data. The only obvious explanation for all these results is that the population of the HeI 2¹P level is not as small for these PN as predicted by Cloudy. It is not the ionisation structure that is wrong though, since the model does predict the strength of the neutral [OI] 6300Å line correctly (at a level between 1 and 5% of H β for these PN). Therefore it seems that the only alternative is that the HeI Ly α destruction probability as used in Cloudy is an overestimate (see Ferland 1999 for a fuller discussion of this factor).

The behaviour of the low temperature PN (those with $T_{eff} < 28000\text{K}$) may be easier to understand. Three of the five objects sit within the model bounds, though they again show deviations from the model since BD+30°3639 should have high density and no turbulence, yet is the lowest of the

three. More importantly, two objects lie below the predicted ratio. For all these objects we must of course be cautious as to whether the temperature scale is accurate. A shift of 3000K in temperature (the effective error on the Kaler & Jacoby relation), would be sufficient to explain all the data. It should also be borne in mind that we may have ‘errant’ observational values for CRL 618 given the comments in section 4.3. Also these PN are unlikely to be well matched by black body stellar atmospheres (BD+30°3639 is a WC star after all). The predicted ratio from the Kurucz models we calculated dropped off more sharply with decreasing effective temperature for example (in the same sense that the [OIII]/H β ratio declines more sharply than for a black body stellar atmosphere, as shown in Figure 7).

Finally we come to the group of objects between 28000 and 40000K. Again there seems to be no direct correlation between the limits on the turbulent velocities and the observed line ratio in contradiction with the models. The two most discrepant points here though are M 1-6 and M 1-14. At least for the these there is observational evidence for moderately high density. M 1-6 may simply have the wrong assigned effective temperature as well, since it is the only object for which we have had to rely on the Acker et al. (1992) catalogue for the 5007Å [OIII] flux. In addition, there is some evidence here for an enhanced helium abundance, since Figure 11 shows that some of the PN that sit above the maximum model value in Figure 10 lie well within the model boundaries of the HeI 2¹P–2¹S to HeI 7^{1,3}G–4^{1,3}F ratio. M 1-6, M 1-9 and M 1-14 are possible examples where this is true (and we note that the first two of these PN are listed as having large helium abundances, and being Peimbert Type I objects, by Shibata & Tamura 1985). We also note however that there are other objects with similar effective temperatures that have even higher observed HeI 2¹P–2¹S to HI Br γ ratios than M 1-14, such as the ultracompact HII region, G45.12+0.13, which again has high density (Lumsden & Puxley 1996). Therefore, two plausible arguments present themselves here: either there is some enhancement to the helium abundance over the 10% assumed in our modelling (as might be expected for Peimbert Type I PN) or the population of the HeI 2¹P level is collisionally enhanced above the maximum values derived using Cloudy (perhaps due to the limited number of triplet states considered in Cloudy). At these values of the effective temperature however there is no need to invoke a change in the HeI Ly α destruction probability.

6 CONCLUSIONS

It is clear from the results we have presented here that the behaviour of the HeI 2¹P–2¹S line is sufficiently complex that it is not a reliable indicator of stellar effective temperature. The variation of 30% or more in both observed and model predictions for a fixed temperature mean that only a very general picture of the effective temperature can be gained from this ratio. It is possible that in certain restricted circumstances, such as objects with known density and turbulent velocity fields, that it may provide secondary information about the effective temperature however. Figure 11 provides an example of how it might be used in combination with another HeI recombination line to constrain the

temperature of objects above 40000K, where the HeI/HI recombination line ratio alone is no longer varying rapidly. However, for this to be reliable the discrepancies between model and data seen in our results will need to be explained. There are factors that we have not accounted for that may help explain some of observations. A change in the dust-to-gas ratio, clumping within the ionised gas or a density rather than ionisation bounded nebula could plausibly explain some of the discrepancies we see. We would certainly not recommend the use of this line however as a primary indicator of stellar effective temperature.

By contrast, the behaviour of the HeI $7^{1,3}\text{G}-4^{1,3}\text{F}$ line, which should be due solely to recombination, is as expected, and in agreement with the models. Although this line is not in itself of particular value, since it is blended with HI Br γ at intermediate spectral resolution, it does show that the use of such HeI lines is in accord with the original intent of Doyon et al. (1992). In particular, the $1.7007\mu\text{m}$ $4^3\text{D}-3^3\text{P}$ transition is also expected to be due mostly to recombination, is in a clear part of the atmospheric H band window, and is well separated from other emission lines. This line has been discussed in the past in this context (eg, Lumsden & Puxley 1996, Vanzi & Rieke 1997). We shall discuss it further in the paper presenting our low resolution spectra for this PN sample.

ACKNOWLEDGMENTS

We would like to thank Derck Smits for providing the machine readable version of his HeI predictions from his 1996 paper. SLL acknowledges support from PPARC through the award of an Advanced Research Fellowship. SLL also thanks the Access to Major Research Facilities Program, administered by the Australian Nuclear Science and Technology Organisation on behalf of the Australian Government, for travel support for the observations reported here. The United Kingdom Infrared Telescope is operated by the Joint Astronomy Centre on behalf of PPARC.

References

Acker, A., Ochsenbein, F., Stenholm, B., Tylenda, R., Marcout, J., Schohn, C., 1992, Strasbourg-ESO Catalogue of Galactic Planetary Nebulae, ESO

Aller, L.H., Keyes, C.D., 1987, ApJS, 65, 405

Aller, L.H., Czyzak, S.J., 1979, Ap&SS, 62, 397

Aller, L.H., Czyzak, S.J., 1983, ApJS, 51, 211

Aller, L.H., Hyung, S., 1995, MNRAS, 276, 1101

Baessgen, M., Hopfensitz, W., Zweigle, J., 1997, A&A, 325, 277

Benjamin, R.A., Skillman, E.D., Smits, D.P., 1999, ApJ, 514, 307

Cahn, J.H., Kaler, J.B., Stanghellini, L., 1992, A&AS, 94, 399

Costa, R.D.D., Chiappini, C., Maciel, W.J., de Freitas Pacheco, J.A., 1996, A&AS, 116, 249

Cuisinier, F., Acker, A., Koppen, J., 1996, A&A, 307, 215

Depoy, D.L., Shields, J.C., 1994, ApJ, 422, 187

Doherty, R.M., Puxley, P.J., Doyon, R., Brand, P.W.J.L., 1994, MNRAS, 268, 821

Doherty, R.M., Puxley, P.J., Lumsden, S.L., Doyon, R., 1995, MNRAS, 277, 577

Dopita, M.A., Meatheringham, S.J., 1991, ApJ, 367, 115

Dopita, M.A., Vassiliadis, E., Meatheringham, S.J., Bohlin, R.C., Ford, H.C., Harrington, J.P., Wood, P.R., Stecher, T.P., Maran, S.P., 1996, ApJ, 460, 320

Dopita, M.A., Hua, C.T., 1997, ApJS, 108, 515

Doyon, R., Puxley, P.J., Joseph, R.D., 1992, ApJ, 397, 117

Ferland, G.J., 1999, ApJ, 512, 247

Ferland, G.J., 1996, Hazy, a Brief Introduction to Cloudy, University of Kentucky Department of Physics and Astronomy Internal Report.

Hora, J.L., Latter, W.B., Deutsch, L.K., 1999, ApJS, 124, 195

Johnson, H.L., 1966, ARA&A, 4, 193

Kaler, J.B., 1985, ApJ, 290, 531

Kaler, J.B., Jacoby, G.H., 1991, ApJ, 372, 215

Kaler, J.B., Bell, D., Hayes, J., Stanghellini, L., 1993, PASP, 105, 599

Kaler, J.B., Kwinter, K.B., Shaw, R.A., Browning, L., 1996, PASP, 108, 980

Kaler, J.B., Shaw, R.A., Browning, L., 1997, PASP, 109, 289

Kelly, D.M., Latter, W.B., Rieke, G.H., 1992, ApJ, 395, 174

Keyes, C.D., Aller, L.H., Feibelman, W.A., 1990, PASP, 102, 59

Kingsburgh, R.L., Barlow, M.J., 1994, MNRAS, 271, 257

Kurucz, R.L., 1992, IAU Symposium 149: The Stellar Populations of Galaxies, eds Barbuy, B., Renzini, A., Kluwer, Dordrecht, Holland, p.225

Kwitter, K.B., Henry, R.B.C., 1998, ApJ, 493, 247

Leitherer, C., 1998, ASP Conf. Ser. 142: The Stellar Initial Mass Function (38th Herstmonceux Conference), 61

Lumsden, S.L., Puxley, P.J., Doherty, R.M., 1994, MNRAS, 268, 821

Lumsden, S.L., Hoare, M.G., 1996, ApJ, 464, 272

Lumsden, S.L., Puxley, P.J., 1996, MNRAS, 281, 493

Mihalas, D., 1972, Non-LTE Model Atmospheres for B and O Stars, NCAR-TN/STR-76

Peimbert M., Torres-Peimbert S., 1983, IAU Symp. 103: Planetary Nebulae, 103, 233

Sabbadin, F., Cappellaro, E., Turatto, M., 1987, A&A, 182, 305

Sahai, R., Trauger, J.T., 1998, ApJ, 116, 1357

Seaton, M.J., 1979, MNRAS, 187, 73P

Shaw, R.A., Kaler, J.B., 1989, ApJS, 69, 495

Shibata, K., Tamura, S., 1985, PASJ, 37, 325

Shields, J.C., 1993, ApJ, 419, 181

Smits, D.P., 1996, MNRAS, 278, 683

Storey, P.J., Hummer, D.G., 1995, MNRAS, 272, 41

Tamura, S., Shaw, R.A., 1987, PASP, 99, 1264

Trammell, S.R., Dinerstein, H.L., Goodrich, R.W., 1993, ApJ, 402, 249

Vanzi, L., Rieke, G.H., 1997, ApJ, 479, 694

Vassiliadis, E., Wood, P.R., 1993, ApJ, 413, 641

Name	Size	T(Stoy)	T(HeII)	[OIII]/H β	HeI/H β	HeII/H β	T _e (K)	n _e (cm ⁻³)	Ref.
BD+303639	8	25600		0.07	0.009		9000	22000 ⁺²⁰⁰⁰⁰ ₋₂₅₀₀	a
CRL 618	10	25600		0.04	0.013			5500 \pm 1000	bc
DdDm 1	1	40000		4.53	0.040		12000	4000 \pm 1000	d
Hu 1-2	8	51000	>250000	7.86	0.029	0.89	16000	4500 \pm 1000	efg
K 3-60	3	73000	220000	14.84	0.028	0.50		4000 \pm 1000	h
K 3-62	3	57800		10.08	0.039		12500	20000 ⁺²⁰⁰⁰⁰ ₋₃₀₀₀	i
K 3-66	0	33100		2.40	0.035		12000	6000 \pm 1000	j
K 3-67	0	59200		10.50	0.039		13800	4500 \pm 1000	hjk
K 4-48	2	65300	>250000	12.40	0.031	0.57	12500	2500 \pm 1000	l
M 1-1	6	37807	>250000	4.37	0.009	1.00	15000	5300 \pm 1000	e
M 1-4	4	66860	83000	12.90	0.032	0.06	12000	5000 ⁺¹⁰⁰⁰ ₋₃₀₀₀	hmn
M 1-6	5	29330		1.22	—			20000 ⁺²⁰⁰⁰⁰ ₋₃₀₀₀	o
M 1-9	12	39900		4.50	0.032		10000	4500 \pm 1000	l
M 1-11	0	25600		0.09	0.008		11400	3000 \pm 1000	klp
M 1-12	0	25890		0.15	0.008		11000	20000 ⁺²⁰⁰⁰⁰ ₋₃₀₀₀	kl
M 1-14	0	34500		2.82	0.037		11500	12000 \pm 1000	q
M 1-20	7	57000		9.80	0.038		11000	20000 ⁺²⁰⁰⁰⁰ ₋₃₀₀₀	pq
M 1-74	5	60700		10.98	0.031		10000	15000 ⁺²⁰⁰⁰⁰ ₋₇₅₀₀	egi
M 1-78	6	35500		3.23	0.031			3500 \pm 1000	hir
NGC 7027	14	70700	190000	14.81	0.029	0.45	13000	20000 ⁺²⁰⁰⁰⁰ ₋₃₀₀₀	hs
PC 12	5	35400		3.03	0.035		10000	7500 ⁺²⁵⁰⁰ ₋₂₅₀₀	lt
SaSt 2-3	0	25500		0.02				2000 \pm 1000	u
Vy 1-1	6	56200		9.60	0.034				i

Table 1: The sample of planetary nebula observed for this project. The Stoy temperatures given are derived from equation 1 of Kaler & Jacoby (1991). T(HeII) is the temperature of the best fitting black-body stellar atmosphere from our modelling (Section 5) for the observed HeII line strength. It is a more accurate estimate of the stellar effective temperature for those objects with HeII emission than the Stoy temperature. Where T_e is not given we assume T_e = 10000K. Where n_e is not given we assume n_e = 5000cm⁻³. Errors in T_e are estimated at approximately 1000K. The optical line ratios are derived from the references given. The ratios tabulated are for 5007Å [OIII]/H β , 6678Å HeI/H β and 4686Å HeII/H β . These are as follows: (a) Aller & Hyung 1995; (b) Baessgen, Hopfensitz & Zweigle (1997); (c) Kelly, Latter & Rieke (1992); (d) Kwitter & Henry (1998); (e) Aller & Czyzak (1979); (f) Sabaddin, Cappellaro & Turatto (1987); (g) Aller & Czyzak (1983); (h) Aller & Keyes (1987); (i) our own data; (j) Tamura & Shaw (1987); (k) Kingsburgh & Barlow (1994); (l) Cuisinier, Acker & Koppen (1996); (m) Aller (1984) as reported in Kaler, Shaw & Browning (1997); (n) Kaler (1985); (o) Acker et al. (1989); (p) Kaler, Kwitter, Shaw & Browning (1996); (q) Costa et al. (1996); (r) Kaler et al. (1993); (s) Keyes, Aller & Feibelman 1990; (t) Shaw & Kaler (1989); (u) Dopita & Hua (1997);

Name	$F(Br\gamma \ (2.166\mu m))$	$I(HeI \ (2.06\mu m))/I(Br\gamma)$	$I(HeI \ (2.11\mu m))/I(Br\gamma)$	$I(HeI \ (2.166\mu m))/I(Br\gamma)$	$I(HeII(2.189\mu m))/I(Br\gamma)$	Corrn.
BD+30°3639	449 ± 0.2	0.294 ± 0.001		0.013 ± 0.001		0.9531
CRL 618	0.36 ± 0.03	0.150 ± 0.100				0.9785
DdDm 1	3.10 ± 0.03	0.786 ± 0.001	0.077 ± 0.001			1.1991
Hu 1-2	17.8 ± 0.2	0.366 ± 0.003	0.067 ± 0.001		0.140 ± 0.006	1.0139
K 3-60	17.3 ± 0.2	0.197 ± 0.001	0.055 ± 0.001	0.029 ± 0.004	0.121 ± 0.011	0.8490
K 3-62	67.3 ± 0.1	0.723 ± 0.001	0.054 ± 0.001	0.047 ± 0.002		1.1341
K 3-66	$7.09 \pm .04$	0.987 ± 0.007	0.035 ± 0.001	0.030 ± 0.008		1.0963
K 3-67	11.1 ± 0.01	0.508 ± 0.001	0.071 ± 0.001	0.044 ± 0.004		1.0544
K 4-48	6.80 ± 0.03	0.418 ± 0.002	0.078 ± 0.001		0.037 ± 0.004	1.0592
M 1-1	1.87 ± 0.03	0.050 ± 0.001	0.031 ± 0.001		0.300 ± 0.017	
M 1-4	25.2 ± 0.03	0.440 ± 0.001	0.068 ± 0.001	0.041 ± 0.007	0.018 ± 0.002	1.0009
M 1-6	47.4 ± 0.05	1.058 ± 0.002	0.034 ± 0.001	0.031 ± 0.002		1.0030
M 1-9	18.3 ± 0.04	1.030 ± 0.004	0.053 ± 0.001	0.053 ± 0.004		0.9970
M 1-11	113 ± 0.1	0.418 ± 0.001	0.010 ± 0.001	0.014 ± 0.002		1.1427
M 1-12	38.4 ± 0.05	0.347 ± 0.001	0.014 ± 0.001	0.017 ± 0.003		0.8114
M 1-14	32.5 ± 0.05	1.132 ± 0.003	0.046 ± 0.001	0.048 ± 0.007		1.0085
M 1-20	27.9 ± 0.05	0.774 ± 0.002	0.050 ± 0.001	0.049 ± 0.004		1.0415
M 1-74	39.2 ± 0.2	0.562 ± 0.003	0.046 ± 0.001	0.049 ± 0.003		0.9119
M 1-78	85.1 ± 0.2	0.787 ± 0.002	0.052 ± 0.001	0.042 ± 0.002		0.9586
NGC 7027	995 ± 0.2	0.279 ± 0.001	0.075 ± 0.001	0.035 ± 0.001	0.138 ± 0.001	0.9427
PC 12	18.8 ± 0.08	0.966 ± 0.006	0.038 ± 0.001	0.037 ± 0.004		1.2120
SaSt 2-3	$3.21 \pm .05$	0.153 ± 0.002				1.1233
Vy 1-1	7.3 ± 0.1	0.332 ± 0.005	0.049 ± 0.001	0.044 ± 0.011		1.1965

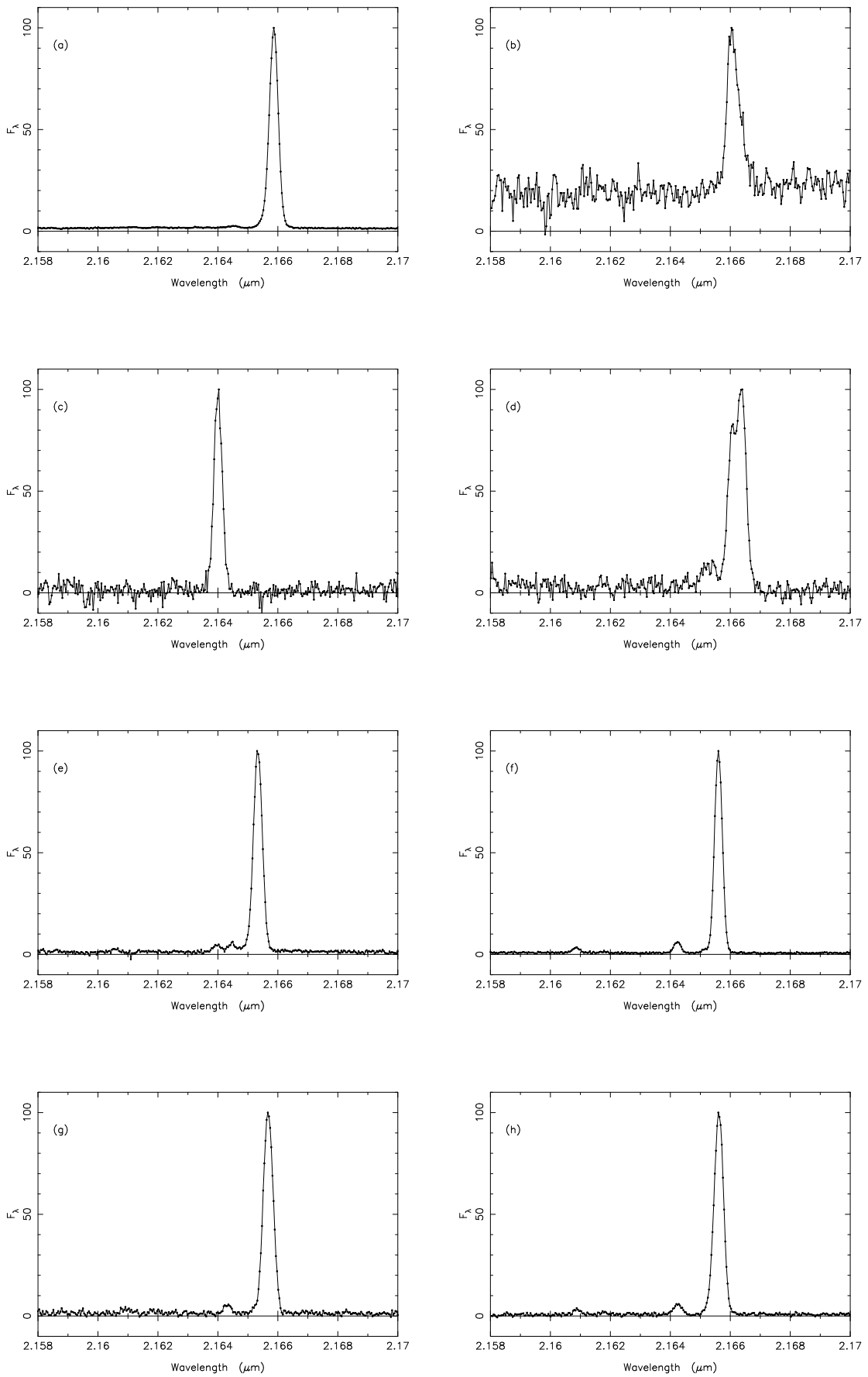
Table 2: Observed HI $Br\gamma$ fluxes, and ratios of the various helium lines with $Br\gamma$ for the planetary nebula sample. The HeI lines tabulated are $2.058\mu m \ 2^1S-2^1P$, $2.113\mu m \ 4^{3,1}S-3^{3,1}P$ and $2.165\mu m \ 7^{1,3}G-4^{3,1}F$. The HeII line is the $2.189\mu m \ 10-7$ transition. The $Br\gamma$ fluxes are in units of $10^{-17}Wm^{-2}$.

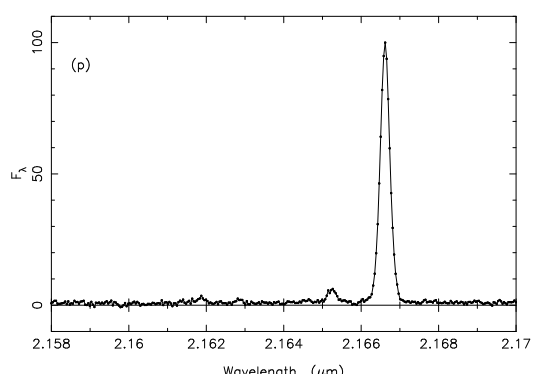
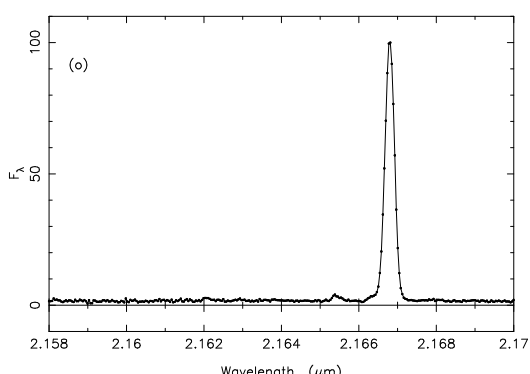
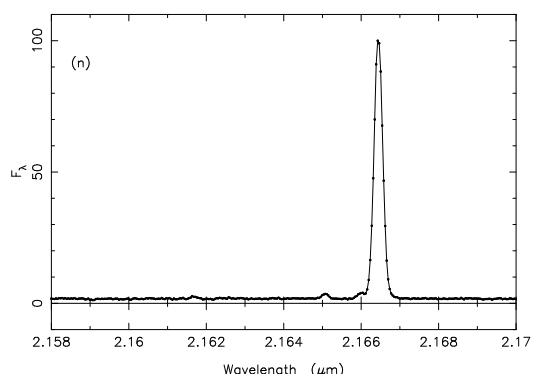
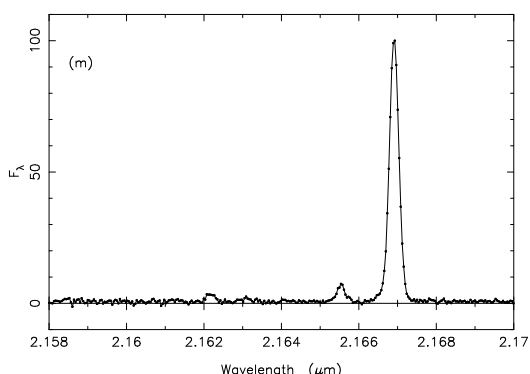
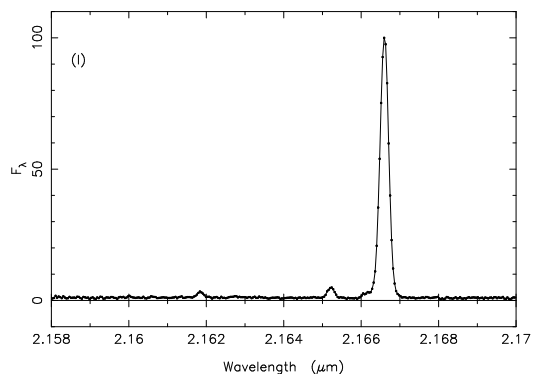
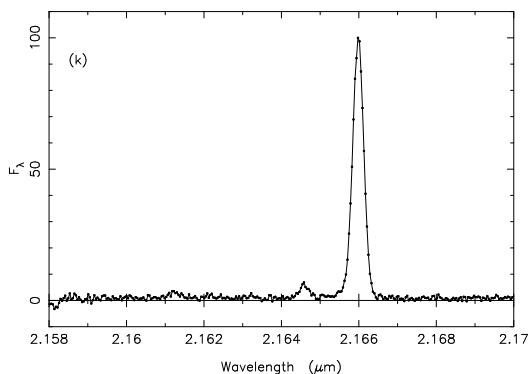
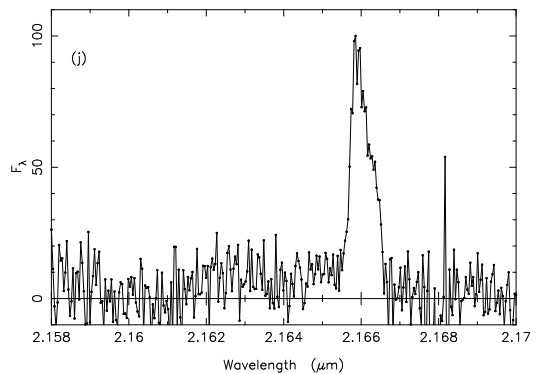
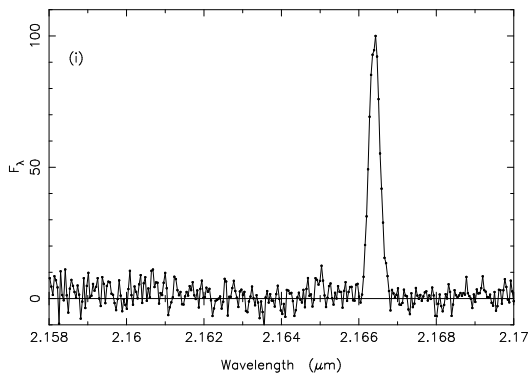
Name	Line Width ($km s^{-1}$)		Name	Line Width ($km s^{-1}$)	
	HI $Br\gamma$	HeI 2^1S-2^1P		HI $Br\gamma$	HeI 2^1S-2^1P
BD+30°3639	42.80 ± 0.69	51.17 ± 0.29	M 1-4	39.33 ± 0.69	30.47 ± 0.58
BD+30°3639		48.40 ± 4.37	M 1-6	26.73 ± 0.69	14.87 ± 0.29
CRL 618	65.09 ± 4.15	40.52 ± 7.29	M 1-9	31.30 ± 0.69	22.30 ± 0.29
DdDm 1	39.75 ± 1.11	34.11 ± 2.92	M 1-11	26.59 ± 0.69	10.64 ± 0.29
Hu 1-2	41.00 ± 2.91	29.30 ± 1.31	M 1-12	30.89 ± 0.69	23.76 ± 0.44
Hu 1-2	39.33 ± 2.91	23.47 ± 0.44	M 1-14	33.10 ± 0.69	26.38 ± 0.29
K 3-60	42.52 ± 0.14	39.21 ± 1.31	M 1-20	27.28 ± 0.14	20.55 ± 0.15
K 3-62	35.87 ± 0.14	34.26 ± 0.15	M 1-74	39.47 ± 0.14	33.24 ± 0.29
K 3-66	47.23 ± 0.83	47.52 ± 0.29	M 1-78	49.72 ± 0.14	48.69 ± 1.02
K 3-67	44.60 ± 0.69	37.76 ± 0.44	NGC 7027	42.93 ± 0.28	41.25 ± 0.15
K 4-48	37.39 ± 1.38	31.78 ± 2.92	PC 12	33.79 ± 0.14	16.03 ± 0.29
M 1-1	53.32 ± 6.92		SaSt 2-3	26.87 ± 1.38	7.29 ± 7.29
M 1-1	45.70 ± 2.46		Vy 1-1	30.47 ± 0.83	25.66 ± 0.73

Table 3: Observed widths of the HI $Br\gamma$ and HeI 2^1P-2^1S lines. For M 1-1 and BD+30°3639, two component Gaussian fits were required for the HI and HeI lines respectively. The values in the table are for the blue and red lines respectively. Empty entries indicate that an object was not observed with the echelle grating for that line, with the exception of BD+30°3639, where the HI line was well fit by a single Gaussian.

Name	HI		HeI	
	v_{turb} (km s^{-1})	v_{exp} (km s^{-1})	v_{turb} (km s^{-1})	v_{exp} (km s^{-1})
BD+30°3639	see comments in text			
CRL 618	see comments in text			
DdDm 1	21	20	20	20
Hu 1-2	see comments in text			
K 3-60	23	22	23	22
K 3-62	18	18	20	18
K 3-66	27	25	29	25
K 3-67	25	23	23	21
K 4-48	20	20	18	16
M 1-1	see comments in text			
M 1-4	21	20	17	15
M 1-6	14	14	9	9
M 1-9	15	15	12	12
M 1-11	13	13	5	5
M 1-12	15	15	14	14
M 1-14	18	18	15	15
M 1-20	13	13	11	11
M 1-74	28	25	28	25
M 1-78	27	25	27	25
NGC 7027	23	22	23	22
PC 12	17	17	8	8
SaSt 2-3	15	15	0	0
Vy 1-1	15	15	15	15

Table 3: Derived upper limits on the turbulent and expansion velocity components from our data.





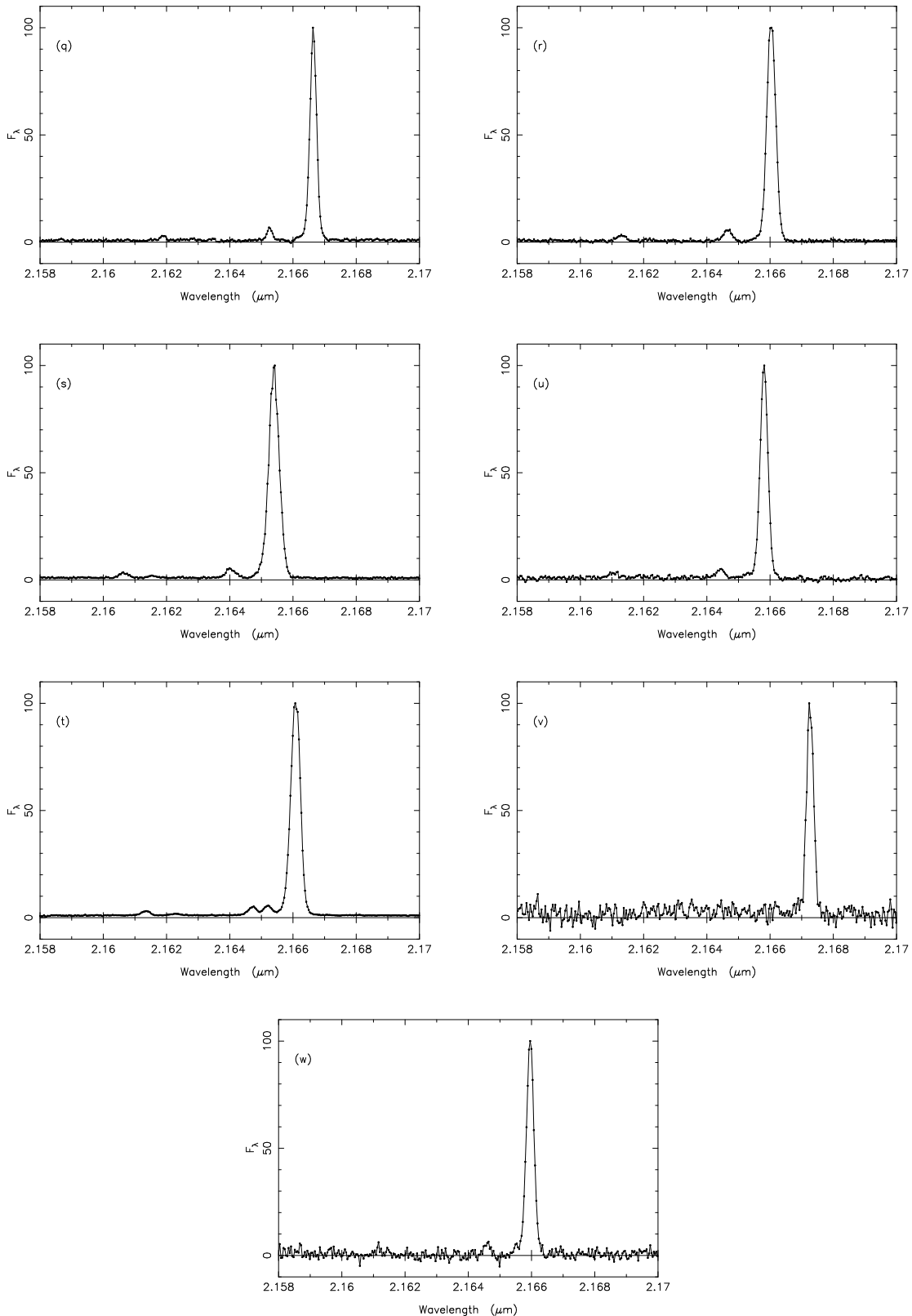
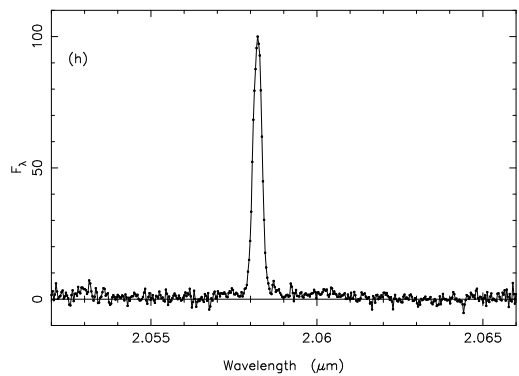
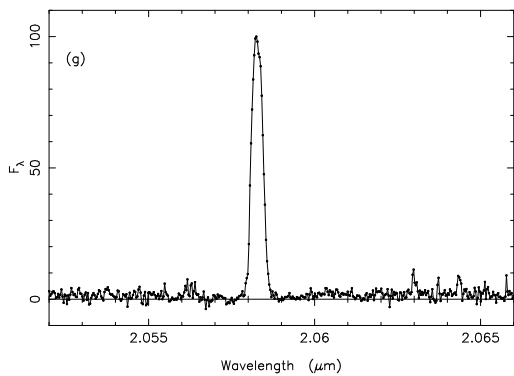
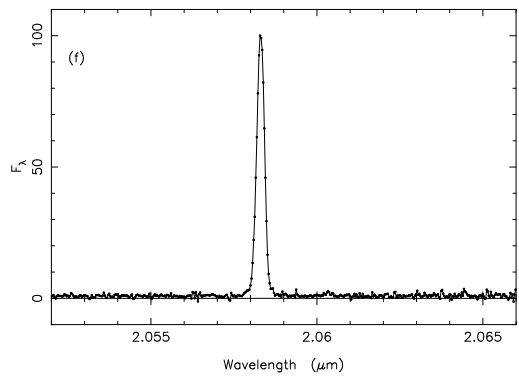
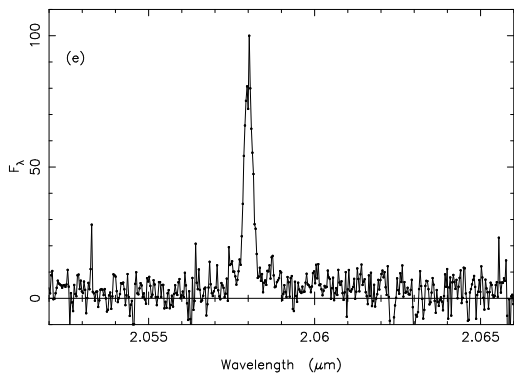
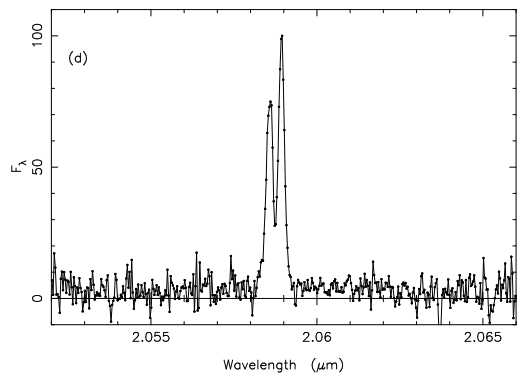
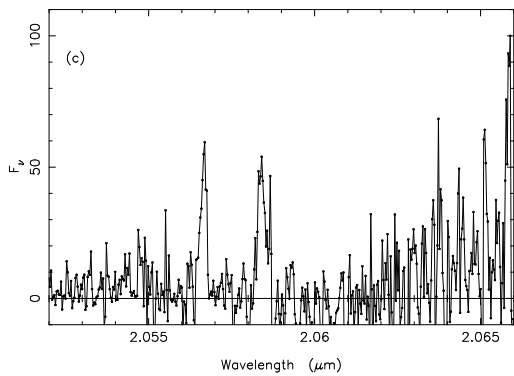
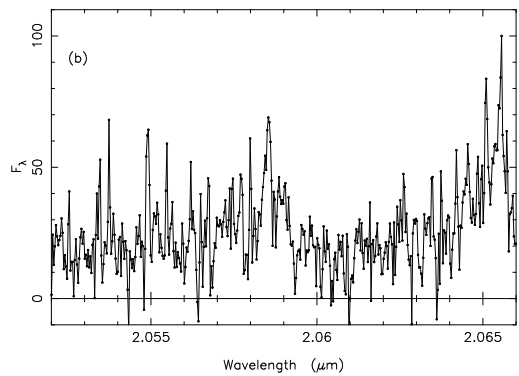
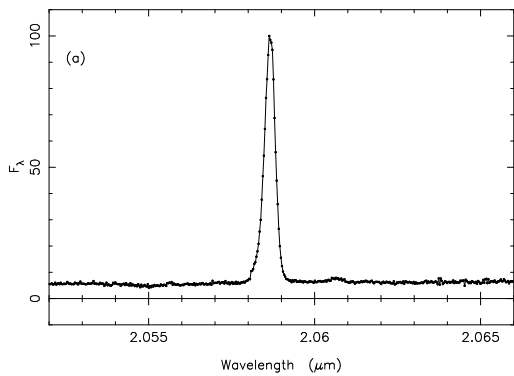
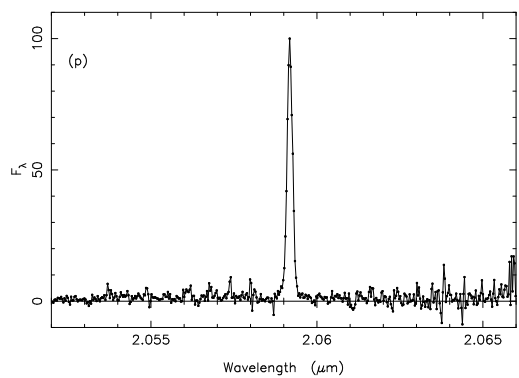
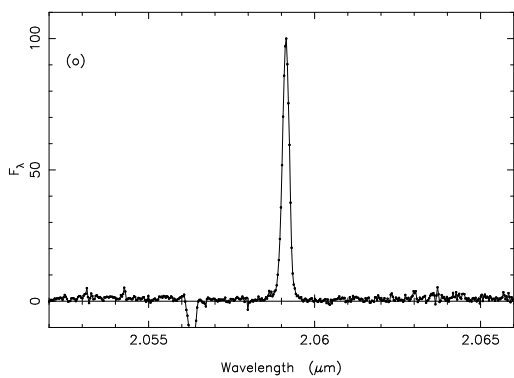
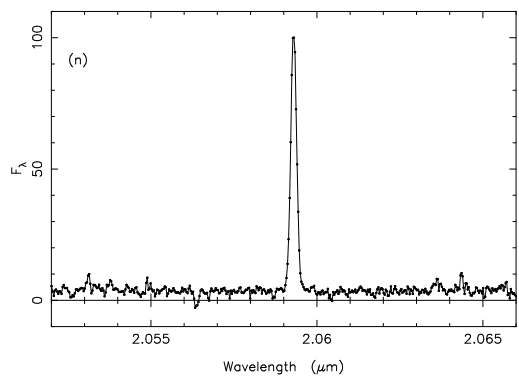
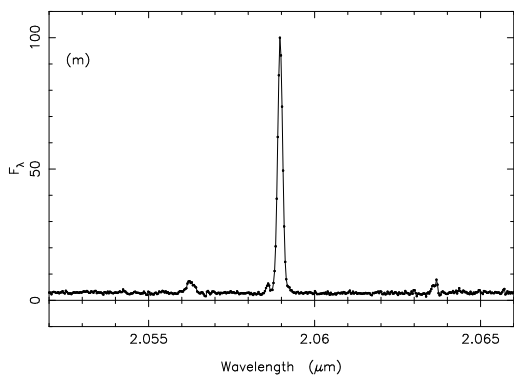
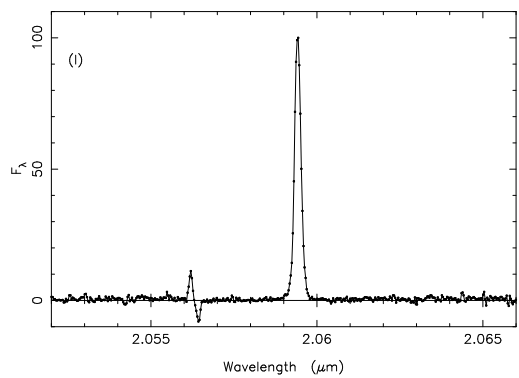
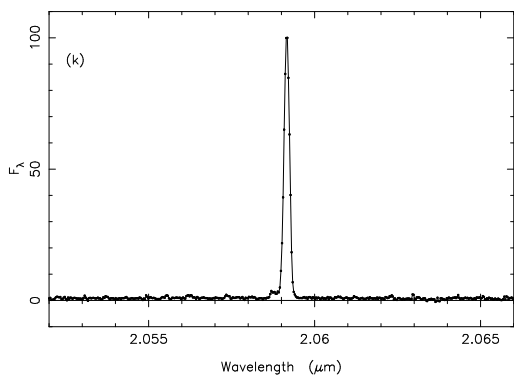
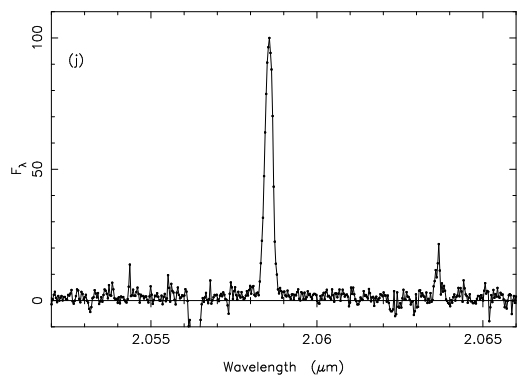
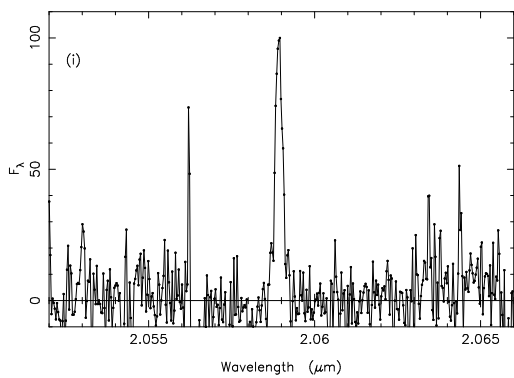


Figure 1: The HI Br γ echelle spectra. The most common of the satellite lines is the 2.16475 μ m HeI 7 1,3 G–4 1,3 F blend. Also visible in some of the spectra are the other HeI transitions of 7 1 F–4 1 D at 2.16229 μ m and 7 3 F–4 3 D at 2.16137 μ m, and the HeII 14–8 transition at 2.1653 μ m. The spectra are of: (a) BD+303639; (b) CRL 618; (c) DdDm 1; (d) Hu 1-2; (e) K 3-60; (f) K 3-62; (g) K 3-66; (h) K 3-67; (i) K 4-48; (j) M 1-1; (k) M 1-4; (l) M 1-6; (m) M 1-9; (n) M 1-11; (o) M 1-12; (p) M 1-14; (r) M 1-74; (s) M 1-78; (t) NGC 7027; (u) PC 12; (v) SaSt 2-3; (w) Vy 1-1.





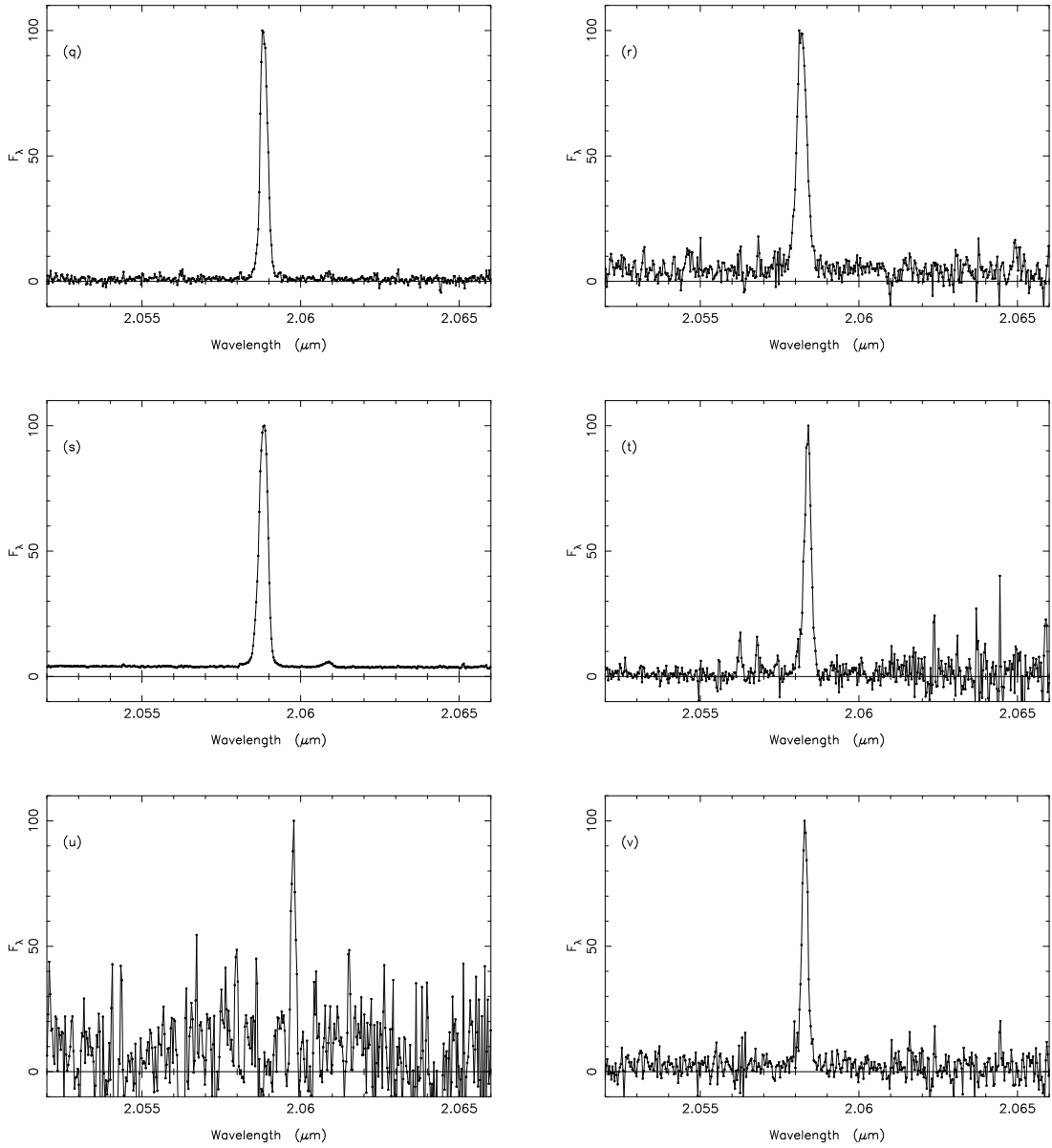


Figure 2: The HeI 2^1P – 2^1S echelle spectra. The spectra are of: (a) BD+303639; (b) CRL 618; (c) DdDm 1; (d) Hu 1-2; (e) K 3-60; (f) K 3-62; (g) K 3-66; (h) K 3-67; (i) K 4-48; (j) M 1-4; (k) M 1-6; (l) M 1-9; (m) M 1-11; (n) M 1-12; (o) M 1-14; (p) M 1-74; (q) M 1-78; (r) NGC 7027; (s) PC 12; (t) SaSt 2-3; (u) Vy 1-1.

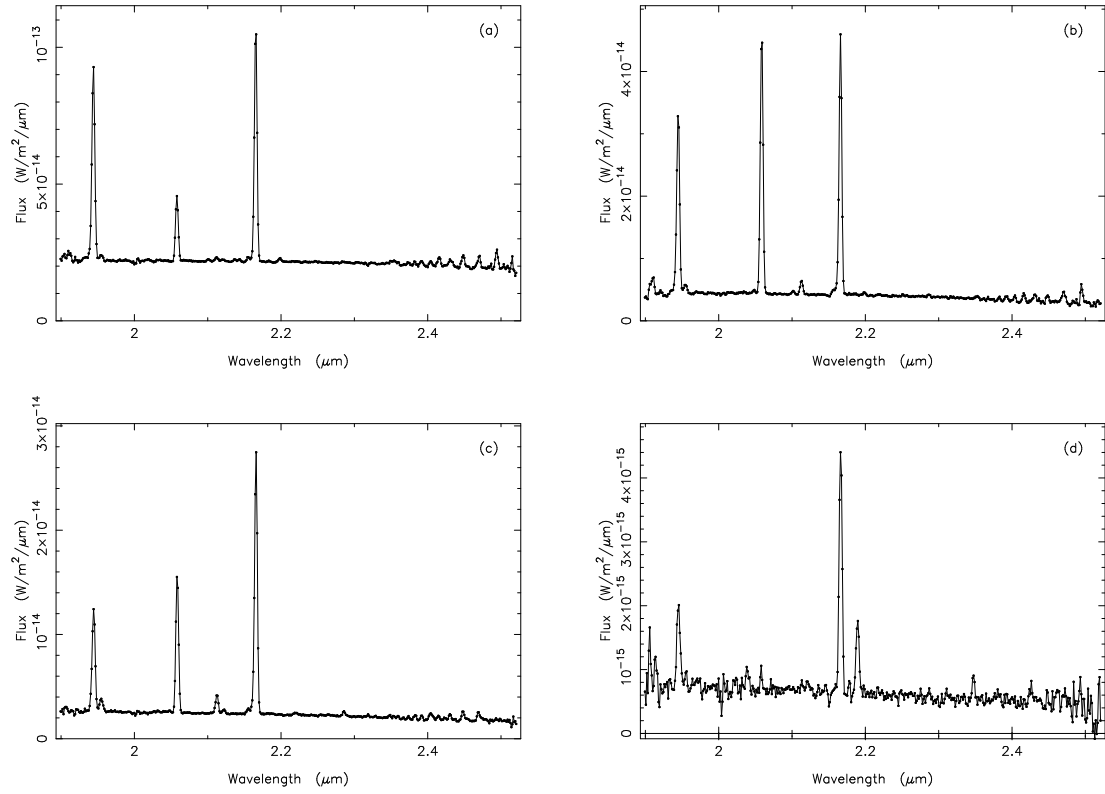


Figure 3: Typical low resolution spectra of the sample. The objects shown are (in order of increasing excitation) (a) M 1-12, (b) M 1-9, (c) K 3-67 and (d) M 1-1. The brightest lines are HI Br γ and Br δ at 2.1661 μ m and 1.9451 μ m respectively, and HeI 2¹S–2¹P at 2.058 μ m. The bright line to the red of Br γ in M 1-1 is HeII 10–7 at 2.1891 μ m, indicative of the very high central star temperature in this object.

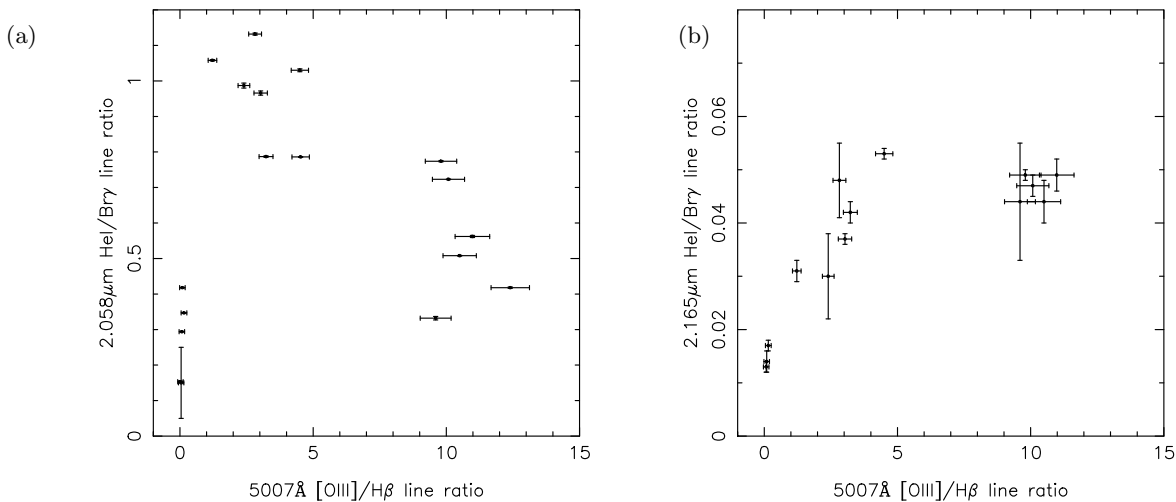


Figure 4: The observed ratios of (a) 2.166 μ m 7^{1,3}G–4^{3,1}F with Br γ and (b) 2.058 μ m 2¹S–2¹P with Br γ against 5007 \AA [OIII] with H β . Note the well defined trend of the data in (a) against the much more complex behaviour shown in (b). This illustrates the difference between a HeI line arising purely from recombination and the 2¹S–2¹P transition.

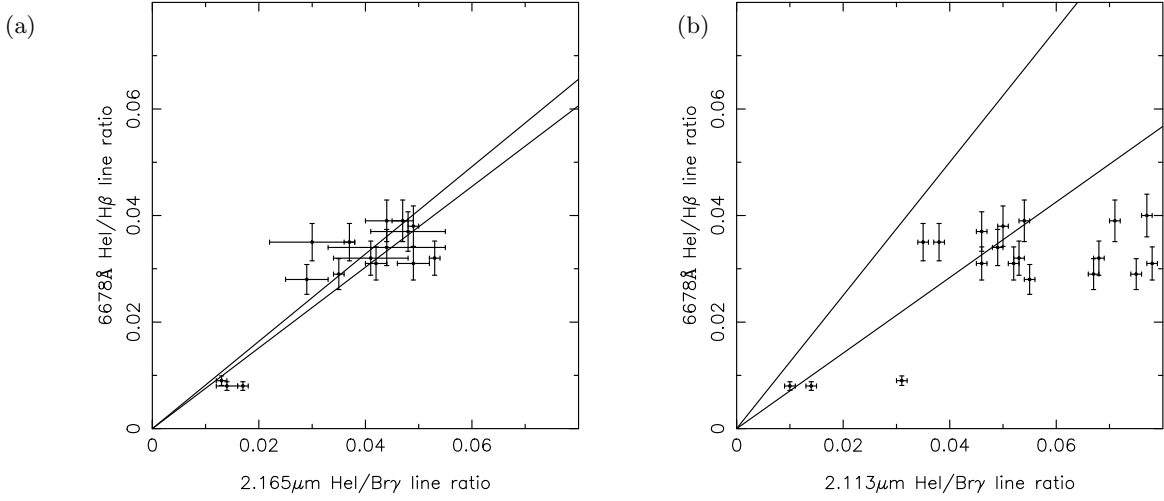


Figure 5: The observed ratios of 6678Å 3^1F – 2^1D with $\text{H}\beta$ plotted against (a) 2.166 μm $7^{1,3}\text{G}$ – $4^{3,1}\text{F}$ with $\text{Br}\gamma$ and (b) 2.113 μm $4^{1,3}\text{S}$ – $3^{3,1}\text{P}$ with $\text{Br}\gamma$. Note how the data in (a) follow an essentially linear relation, whereas in (b) there is significant scatter in the relation between the lines. The latter is due to enhancement of the 4^3S level of HeI either through collisions or as a result of significant opacity in the 2^3S – $n^3\text{P}$ series. The solid lines in each figure represent the theoretical bounds for the plotted ratios for the range of electron temperature and density considered.

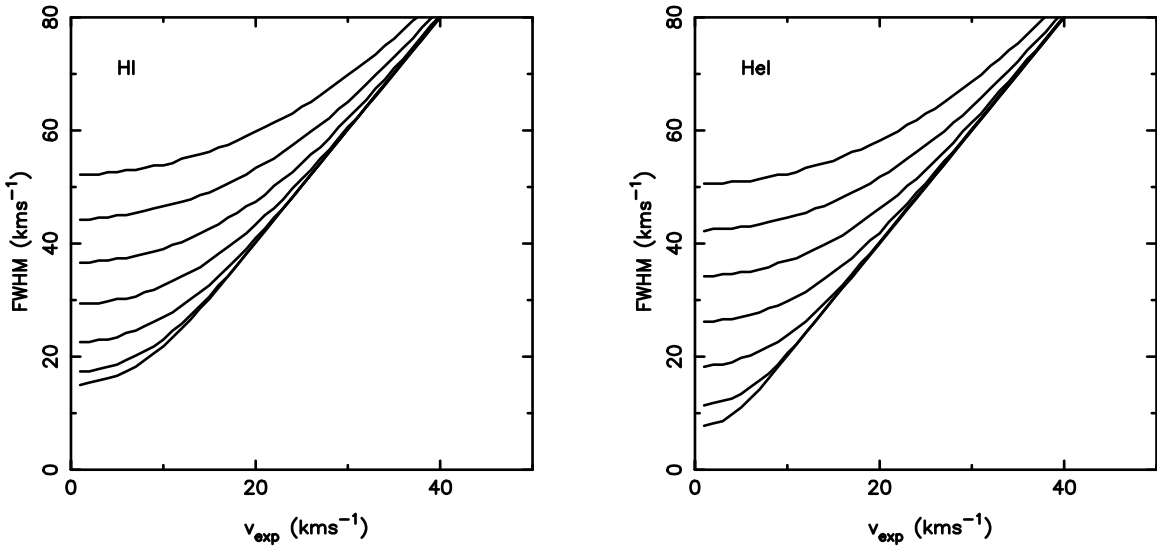


Figure 6: The derived value of the full width at half maximum of the integrated emission line using our simple expansion model as a function of v_{turb} and v_{exp} . The solid curves represent (from bottom up) values of v_{turb} of 0, 5, 10, 15, 20, 25 and 30 km s $^{-1}$.

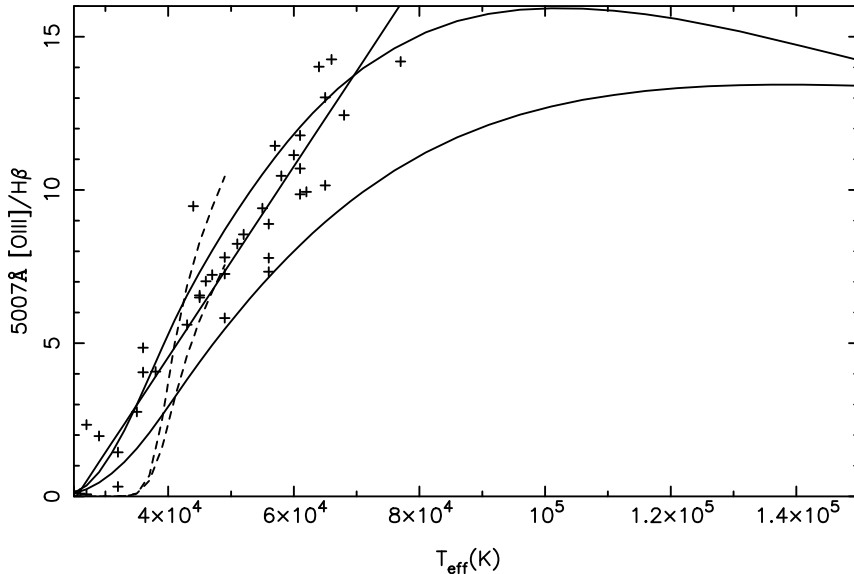


Figure 7: The observed and predicted behaviour of the 5007Å [OIII] to H β ratio as a function of effective temperature. The solid lines are generated using simple blackbodies for the model stellar atmospheres. The dashed lines are generated from Kurucz model atmospheres. The crosses are the data from Kaler & Jacoby (1991), where we have used their tabulated Stoy temperatures for T_{eff} . The straight line is their best fit relation to this data. The two curved lines for each set of models are the extreme values from our grid. The upper line represents the prediction for a central star of luminosity $7000 L_{\odot}$, with electron density of 24000 cm^{-3} , the lower a star of luminosity $3000 L_{\odot}$ and electron density of 3000 cm^{-3} .

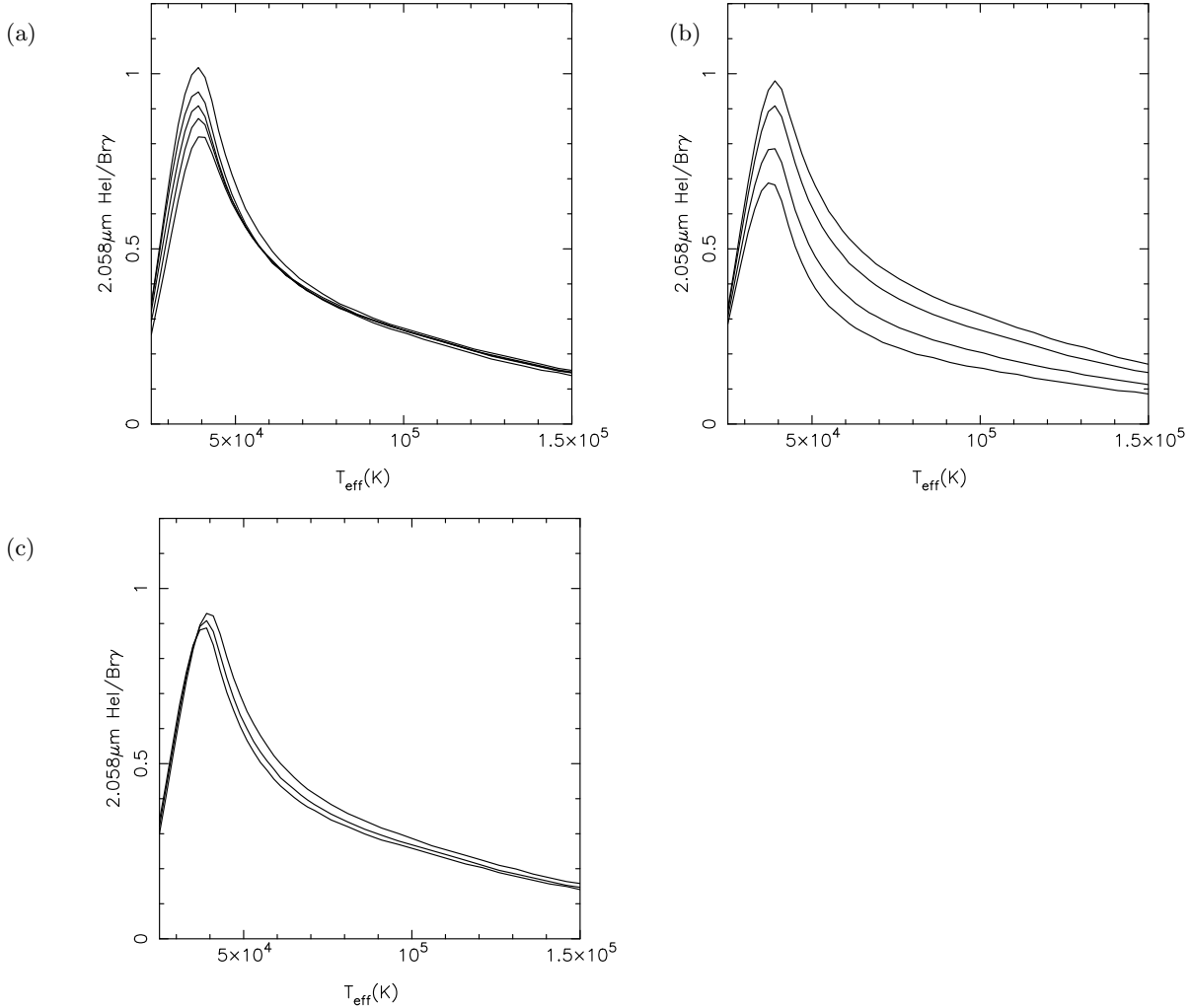


Figure 8: The predicted ratio of the $2.058\mu\text{m}$ HeI 2^1S – 2^1P line with HI $\text{Br}\gamma$ as a function of stellar effective temperature. In (a) we show the dependence on density, in (b) on turbulent velocity and in (c) on central star luminosity. In each case we held the other two parameters constant at the values of $n_e = 12000\text{cm}^{-3}$, $v_{turb} = 5\text{km s}^{-1}$ and $L_* = 5000\text{L}_\odot$. In (a) the curves correspond to $n_e = 3000, 6000, 12000, 24000$ and 48000cm^{-3} from lowest up. In (b) the curves correspond to $v_{turb} = 0, 5, 10$ and 15km s^{-1} from highest down. In (c) the curves correspond to $L_* = 3000, 5000$ and 7000L_\odot from highest down.

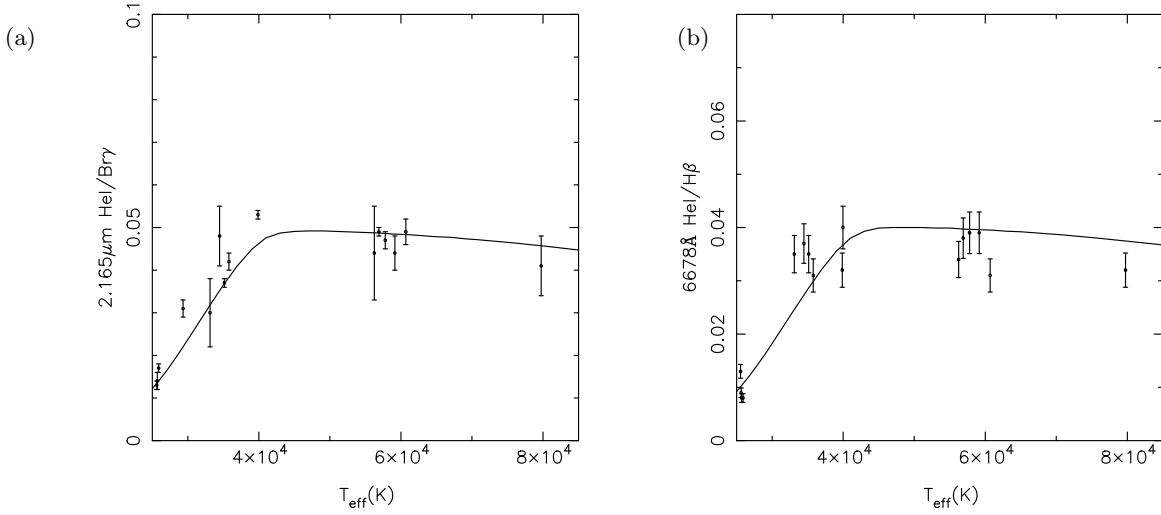


Figure 9: The observed and predicted behaviour of (a) the ratio of the $2.16475\mu\text{m}$ HeI 7^1D – 4^1P line with HI Br γ and (b) the 6678\AA HeI 3^1D – 2^1P with H β as a function of effective temperature. The model plotted has $L_* = 5000 L_\odot$ and $T_e = 10000\text{K}$. There is less than 5% variation of the model ratios with either density or turbulent velocity.

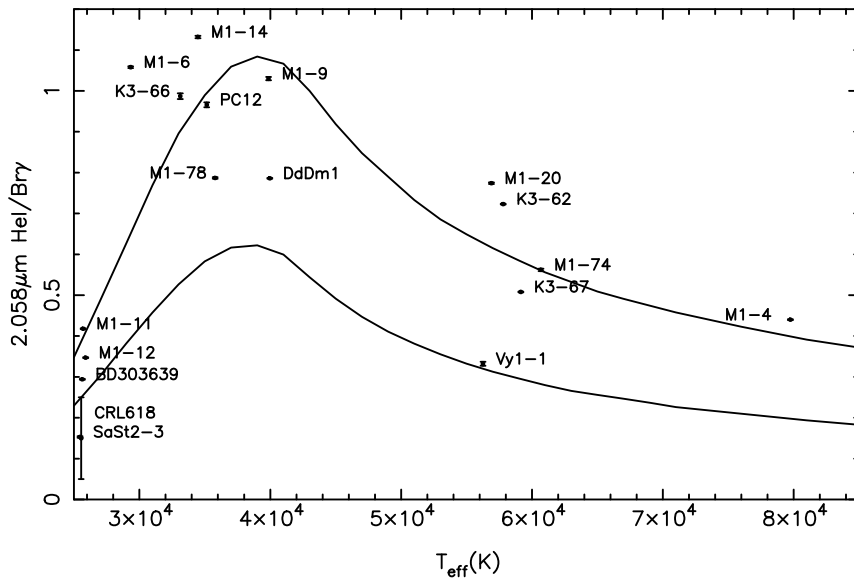


Figure 10: The observed and predicted behaviour of the ratio of the $2.058\mu\text{m}$ HeI 2^1S – 2^1P line with HI Br γ . The models plotted are for $n_e = 48000\text{cm}^{-3}$ and $v_{turb} = 0\text{km s}^{-1}$ (upper curve) and $n_e = 3000\text{cm}^{-3}$ and $v_{turb} = 15\text{km s}^{-1}$ (lower curve) which are essentially the extreme maxima and minima in our model grids. In both cases $L_* = 5000 L_\odot$. T_{eff} is estimated from the observed 5007\AA [OIII] or 4686\AA HeII to H β ratio as discussed in the text.

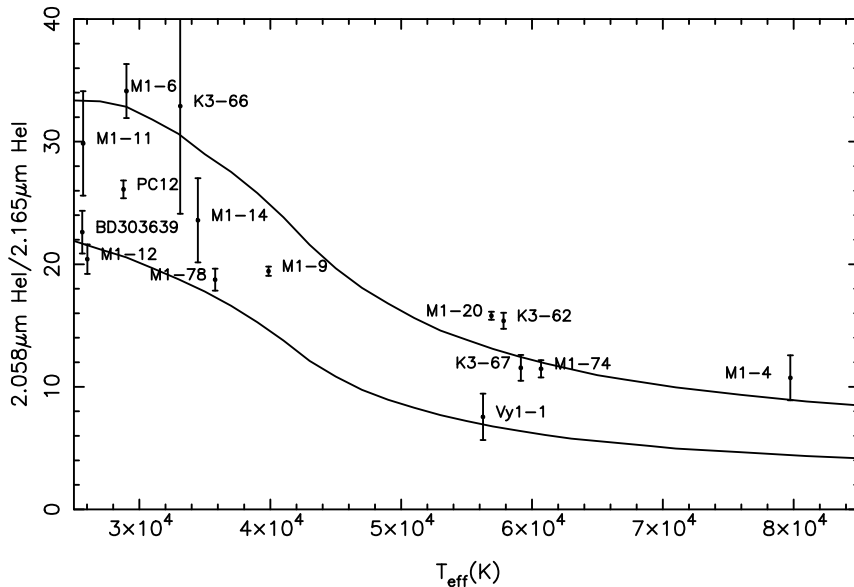


Figure 11: The observed and predicted behaviour of the ratio of the $2.058\mu\text{m}$ HeI 2^1S – 2^1P line with the $2.16475\mu\text{m}$ HeI $7^{1,3}\text{G}$ – $4^{1,3}\text{F}$ line. The models plotted are the same as in Figure 8.